Advances in Water Resources 162 (2022) 104150

Contents lists available at ScienceDirect

Advances in Water Resources

journal homepage: www.elsevier.com/locate/advwatres

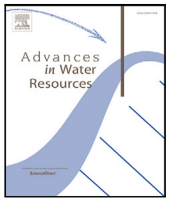

Stable drainage in a gravity field

Stephen J. Breen [a,*,1], Steven R. Pride [b], Yder Masson [c], Michael Manga [a]

[a] Department of Earth and Planetary Science, University of California, Berkeley, United States of America
[b] Energy Geosciences Division, Lawrence Berkeley National Laboratory, United States of America
[c] Team Magique 3D, Inria, E2S UPPA, CNRS, France

ARTICLE INFO

Keywords:
Multiphase flow
Porous media
Hydrogeology
Drainage

ABSTRACT

During drainage, as a voxel of porous material is being actively invaded prior to percolation, the invading nonwetting fluid cannot be transmitted to the neighboring downstream voxel until a critical nonwetting saturation (S_{nc}) is reached. This occurs when the invading fluid forms a percolating path across the voxel. We present novel laboratory observations of gravitationally stable, air/water drainage in thin bead packs, with 2D saturation fields monitored at high spatial and temporal resolution using transmitted light. We also present Invasion Percolation simulations. Both show that S_{nc} has a strong dependence on capillary number (Ca), Bond number (Bo), and voxel size (L_z). We propose a percolation model that describes the functional form of $S_{nc}(\mathrm{Bo}, \mathrm{Ca}, L_z)$. We also produce a new theoretical model for the macroscopic capillary pressure function $P_c(S_w, \mathrm{Bo}, \mathrm{Ca}, L_z)$, where S_w is the saturation of wetting fluid in the voxel.

1. Introduction

A macroscopic, porous-continuum theory of multiphase, immiscible flow in geological materials must provide equations for the spatial and temporal evolution of the saturations and average fluid pressures of each fluid as defined in macroscopic voxels (averaging volumes) that surround each point of the porous material (a voxel, or volume element, is the 3D analog of a pixel, or picture element). Experimental advances in observing meniscus dynamics (e.g., Reynolds et al., 2017) and computational advances in pore-scale, interface-resolving methods (e.g., Abu-Al-Saud et al., 2017) demonstrate the complex pore-scale interfacial dynamics occurring as immiscible fluids advance through a voxel. An ongoing challenge is to capture at the macroscopic scale the pertinent, averaged nature of the actual pore-scale physics during immiscible invasion.

The standard porous-continuum model of two-phase immiscible flow in an isotropic material involves two statements of mass conservation, where the index $i = w, n$ denotes either the wetting w or nonwetting n fluid,

$$\frac{\partial}{\partial t}[\phi S_i \rho_i] = -\nabla \cdot (\rho_i \boldsymbol{q}_i) \tag{1}$$

and two statements of momentum conservation that are written as Darcy transport laws

$$\boldsymbol{q}_i = k_o \frac{\kappa_i(S_w)}{\eta_i}(-\nabla P_i + \rho_i \boldsymbol{g}) \tag{2}$$

where ϕ is porosity, ρ_i average mass density of fluid i in a voxel, S_i saturation of fluid i (the volume of fluid i in a voxel divided by the volume of the pore space), $\boldsymbol{q}_i$ the Darcy velocity of fluid i (the average fluid i velocity relative to the solid framework of grains and multiplied by porosity), P_i the average fluid pressure in phase i, k_o the single-phase permeability of the material, and $\kappa_i(S_w)$ the dimensionless relative-permeability coefficients of each fluid, which are assumed to be functions of saturation S_w.

If porosity remains constant during flow, once the Darcy laws are inserted into the two mass conservation equations, we have two equations for six unknowns: S_n, S_w, ρ_n, ρ_w, P_n and P_w. The remaining four equations are a statement that the pore space is entirely filled by both fluids

$$S_w + S_n = 1, \tag{3}$$

equations of state for each phase, which under isothermal flow conditions are the given monotonic functions $\rho_n(P_n)$ and $\rho_w(P_w)$, and, last, the assumption of a capillary pressure function

$$P_n - P_w = P_c(S_w), \tag{4}$$

where $P_c(S_w)$ is a given monotonic function of saturation. The function $P_c(S_w)$ is typically measured experimentally under equilibrium hydrostatic conditions where S_w changes slowly by small increments in response to controlled P_c changes.

* Corresponding author.
E-mail address: sbreen@uci.edu (S.J. Breen).
[1] now at "Department of Civil and Environmental Engineering, University of California, Irvine, United States of America".

https://doi.org/10.1016/j.advwatres.2022.104150
Received 19 May 2021; Received in revised form 2 October 2021; Accepted 4 February 2022
Available online 22 February 2022

Our focus in this article is whether the above "standard model" of two-phase flow at the continuum scale, including commonly employed forms for the functions $\kappa_w(S_w)$, $\kappa_n(S_w)$ and $P_c(S_w)$, can capture the way that a gas invades a liquid-saturated porous material when the invasion is in the direction of the gravity field, which results in stable drainage fronts. There are several points of concern, and alternative models have been developed to address some of them (e.g. Hassanizadeh and Gray, 1990; Gray and Miller, 2014).

A requirement for the validity of Darcy's law in a given phase i is that the flow of phase i is laminar, which requires that phase i is continuous across each voxel. When a voxel is being drained for the first time prior to percolation, however, the nonwetting fluid is not continuous across the voxel. Rather, it advances by discrete Haines jumps in which the local pressure drop across a meniscus trapped at a constriction in the pore space exceeds a threshold value, allowing the invading fluid to rush forward at relatively high Reynolds number (Re $\sim$ 1) into downstream pores (Armstrong et al., 2015). At each jump, a single initial meniscus separates until all newly formed menisci become trapped at downstream capillary barriers, where they remain until the drainage causes the pressure drop across one of them to exceed the threshold value for that constriction, and another jump occurs. A Darcy law for the invading phase does not apply until percolation for that phase has occurred and laminar flow is taking place along the backbone of nonwetting fluid traversing the voxel. When saturation reaches a steady state, flow is laminar.

Formally, the relative permeability of the invading phase must be zero in a voxel undergoing invasion until the nonwetting saturation of that voxel reaches a critical value, S_{nc}, which corresponds to the nonwetting saturation at the moment of nonwetting-phase percolation across the voxel. In a macroscopic description of drainage, only once the nonwetting saturation is greater than S_{nc} can we begin to allow nonwetting fluid to invade the next downstream voxel according to the newly emergent Darcy's law. Here, we will show that S_{nc} is a function of the Bond (Bo) and capillary (Ca) numbers and the voxel size (L_z), and we will obtain an expression for the function $S_{nc}(\mathrm{Bo}, \mathrm{Ca}, L_z)$. During invasion, the defending wetting phase has a continuous path across the voxel and flows in a laminar manner between Haines jumps, as described by Darcy's law. The fractal nature of the invading fluid structure created in a voxel during the percolation process is incorporated into our model of S_{nc}.

The concept of achieving a critical saturation prior to allowing nonwetting fluid to enter the next downstream voxel is not new. It was initially proposed by Corey (1954) and has been subsequently investigated by Dury et al. (1999), Yortsos et al. (2001) and Ghanbarian et al. (2016), among others. In particular, Dury et al. (1999) conclude: "an adequate description of the nonwetting phase relative permeability function by any model can only be expected if the emergence point of nonzero permeability is correctly represented".

We will show here that during drainage, the one dimensional saturation profile $s(z)$ within a voxel depends on the buoyancy force as quantified by the Bond number (Bo), on the rate of invasion or extraction as quantified by the capillary number (Ca), and on the linear size of the voxel (L_z). We will provide a model for the function $s(z)$ that is consistent with Invasion Percolation concepts. This model for $s(z)$ is then shown to produce a new theoretical prediction for the macroscopic capillary pressure function $P_c(S_w, \mathrm{Ca}, \mathrm{Bo}, L_z)$.

Experiments conducted in bead monolayers and microchannel networks (e.g., Lenormand et al., 1988; Birovljev et al., 1991; Frette et al., 1997; Løvoll et al., 2005; Cottin et al., 2010; Toussaint et al., 2012; Hoogland et al., 2015) demonstrate that the morphology of a drainage front depends on the balance of buoyancy, viscous and capillary forces. The gravitational-pressure drop over a characteristic entry pore size a_0 in the direction $\hat{\mathbf{z}}$ of the average flow is given by $\Delta P_g = a_0 \hat{\mathbf{z}} \cdot \nabla P_g = a_0 \Delta\rho\, \hat{\mathbf{z}} \cdot \mathbf{g}$, where $\Delta\rho = \rho_w - \rho_n$ is the difference in fluid density and $\mathbf{g}$ the acceleration of gravity. Dividing this pressure drop by the capillary pressure drop across a meniscus γ/a_0, where γ is surface tension, defines the Bond number Bo

$$\mathrm{Bo} = \frac{a_0^2 \Delta\rho g\, \hat{\mathbf{z}} \cdot \hat{\mathbf{g}}}{\gamma}. \tag{5}$$

The viscous pressure drop over the pore distance a_0 in the direction of flow $\hat{\mathbf{z}}$ is given by $\Delta P_v = -a_0 \hat{\mathbf{z}} \cdot \nabla P_v = a_0 \eta_w \hat{\mathbf{z}} \cdot \mathbf{q}_w / k_o$, where η_w is the viscosity and $\mathbf{q}_w$ the interstitial velocity of the wetting fluid at the tip of the front. Dividing this viscous pressure drop by the capillary pressure drop across a meniscus defines the capillary number Ca

$$\mathrm{Ca} = \frac{a_0^2 \eta_w \hat{\mathbf{z}} \cdot \mathbf{q}_w}{\gamma k_o}. \tag{6}$$

When Bo $>$ 0, the drainage front is stabilized, and when Bo $<$ 0, unstable gravitational fingers develop. For the drainage case where the invading nonwetting fluid is less viscous than the defending wetting fluid, even when Bo $>$ 0, the tip of the invasion front becomes unstable when Ca becomes sufficiently large compared to Bo, resulting in viscous fingers of similar morphology to gravitational fingers (Glass et al., 2000).

Our work in this study is constrained by novel experimental measurements of gravity-stabilized drainage in a thin 3D bead pack. By continuously measuring light transmission across the thinnest dimension of the bead pack, we obtain 2D maps of how the saturation varies through time, and we compare these results to standard-model numerical simulations using TOUGH2 (Pruess, 2004) when the van Genuchten (1980) model for $P_c(S_w)$ has parameters determined experimentally for our specific flow cell. After demonstrating that the standard model does not accurately predict the observed saturation during invasion, the rest of the paper is dedicated to making modifications to the standard model based on the pore-scale physics of gravity-stabilized drainage at variable Bo and Ca. A table of symbols and notation is provided in Appendix.

2. Experiments and associated simulations

2.1. Laboratory experiments

We perform drainage experiments in translucent, acrylic cells with dimensions 152 mm height, 76 mm width, and 13 mm thickness. The porous material is glass beads with screen size 20/30 (0.59 to 0.84 mm, d_{50} = 0.72 mm), which is similar to a coarse, well-sorted sand. The beads are cleaned with distilled water prior to use. We will characterize a typical entry pore size a_0 (an effective pore diameter) for the bead pack using $a_0 = d_{50}/3$ = 0.24 mm. Prior to assembly, a monolayer of beads is adhered to the inner walls of the cell with a clear, inert glue to prevent preferential flow along bead–wall interfaces. To exclude minor preferential flow in the corners of the cell and entry/exit effects, we record observations over a central region of 65 mm width × 115 mm height. Fig. 1 shows the experimental setup and the inside of a flow cell.

We fill the cells by pouring beads rapidly through a randomizing screen to prevent continuous grain-size sorting. Once full, a vibration motor is attached to the cells and left running until the bead level stabilizes to 150 mm height, which produces a dense, stable, and repeatable packing.

Water flow into or out of the cell is regulated by a syringe pump connected to a manifold at the base. Prior to saturating with water, several pore volumes of CO_2 are passed through to displace air. The high solubility of CO_2 in water ensures that the chamber reaches full water saturation. Distilled water is then injected into the chamber at a slow flow rate, and porosity (ϕ) is calculated by measuring the water level several times during filling, yielding ϕ = 0.31. Once full with water, the flow rate is slightly increased, and several pore volumes of water are passed through to remove any debris or residual CO_2 from the cell. The single-phase permeability (k_o) of the bead pack was measured

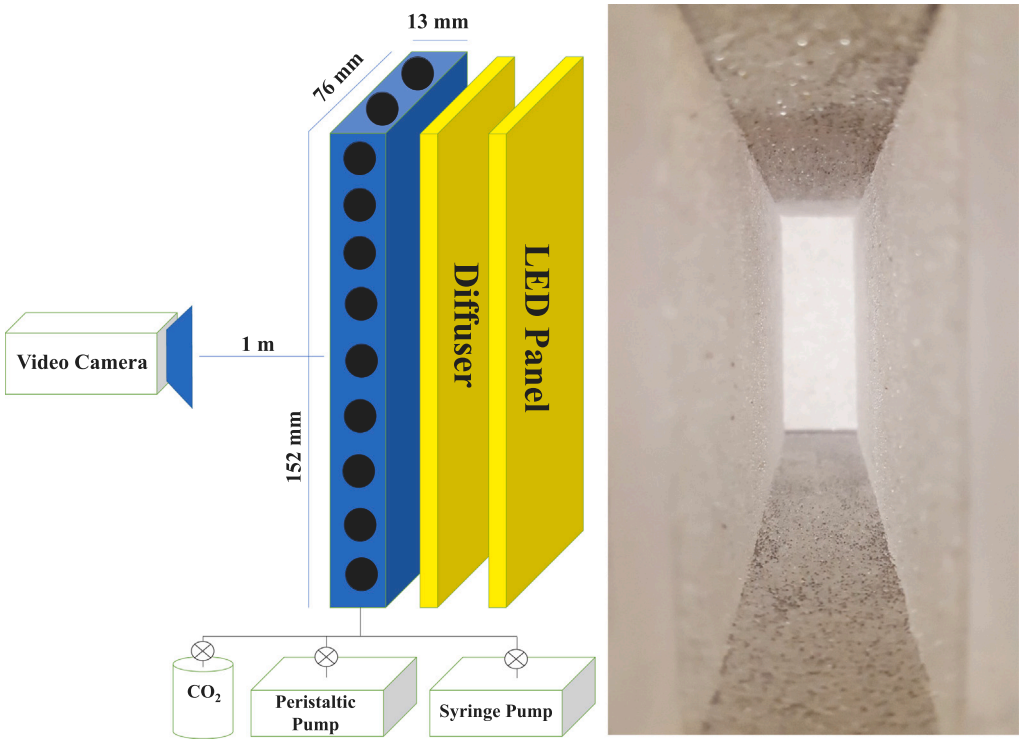

Fig. 1. The experimental apparatus consists of a thin flow cell, a light diffuser, and a 7.5 W LED panel. A monochrome camera records continuously during drainage. A syringe pump is used to steadily withdraw fluid, and a peristaltic pump is used to saturate and flush the chamber with water after displacing air with CO_2. The photograph on the right shows the interior of the flow cell, which is lined with beads to minimize preferential flow along the inner walls.

by the falling head method, yielding $k_o = 1.6 \times 10^{-10}$ m^2. The air–water surface tension at laboratory temperature is $\gamma = 0.072$ Pa m.

Gravitationally-stable drainage (Bo $= 7.4 \times 10^{-3}$) was performed by mounting the cell vertically and imposing a water withdrawal rate at the lower boundary with an atmospheric upper boundary. To observe any capillary number dependencies, a range of drainage flow rates was explored: 1 ml/min (Ca $= 5.0 \times 10^{-5}$), 5 ml/min (Ca $= 2.5 \times 10^{-4}$), 10 ml/min (Ca $= 5.0 \times 10^{-4}$), 15 ml/min (Ca $= 7.5 \times 10^{-4}$), 20 ml/min (Ca $= 1.0 \times 10^{-3}$), 25 ml/min (Ca $= 1.25 \times 10^{-3}$), and 30 ml/min (Ca $= 1.5 \times 10^{-3}$). The largest flow rate corresponds to a Reynolds number of Re $= \rho_w a_0 v_w / \eta_w = 0.37$, which is close to the nonlinear advection regime (Re > 1) where Darcy's law is no longer a very good approximation. Drainage timing begins when the first Haines jump occurs along the upper boundary. All observations were made on a single cell that was not repacked between drainage runs.

We measure saturation with visible light transmission. The light source is a diffused 7.5 W LED panel. A monochrome video camera (Redlake Motionpro) is mounted 1 meter from the cell and captures images continuously. The amount of data that can be recorded during a drainage run is limited by the camera's internal buffer size. We maintain a constant 25 frames per second at a resolution of 17 pixels per centimeter in both dimensions. To relate measured light intensity I at a pixel to the average saturation S_w across the cell at that pixel, the model of Tidwell and Glass (1994) fits our measurements quite well.

Conceptually, if a beam of light of intensity I_o is incident on a layer of glass beads saturated with water and air, its intensity decreases by a transmittance factor each time it traverses from the solid beads into a pore and decreases exponentially with distance traveled in each phase due to absorption. The absorption coefficients in solid, air and water are denoted α_s, α_a and α_w. The normal-incidence transmittance factor at a planar solid–air interface is

$$\tau_{sa} = \frac{4 n_s / n_a}{(n_s/n_a + 1)^2} \tag{7}$$

where n_a is the refractive index of air ($n_a = 1.0$), and n_s is the refractive index of our glass beads ($n_s = 1.54$), which yields $\tau_{sa} = 0.955$. An identical expression exists for the transmittance factor τ_{sw} at a solid–water interface, which with $n_w = 1.33$ yields $\tau_{sw} = 0.991$. If there are an average of k pores traversed on a straight line across the cell such that $k_w = S_w k$ of them are saturated with water and $k_a = (1 - S_w)k$ are saturated with air, the distance traveled through water is $d_w = k_w d_p$, where $d_p \approx d_{50}$ is average pore diameter, the distance through air is $d_a = k_a d_p$, and the distance through solid is denoted d_s. Since each pore experiences two transmittances from solid to pore, we have the following model for the transmitted light intensity I:

$$I = I_o e^{-\alpha_s d_s - \alpha_w d_w - \alpha_a d_a} \tau_{sa}^{2k_a} \tau_{sw}^{2k_w}. \tag{8}$$

Defining I_a to be the transmitted intensity when $S_w = 0$ (fully air-saturated beads) and I_w to be the transmitted intensity when $S_w = 1$, we can rewrite the expression for I as

$$I = I_a e^{-(\alpha_w - \alpha_a) S_w k d_p} \left(\frac{\tau_{sw}}{\tau_{sa}} \right)^{2 S_w k}. \tag{9}$$

Assuming that $\alpha_w \approx \alpha_a$ and introducing the normalized intensity $\tilde{I}$ defined as

$$\tilde{I} = \frac{I - I_a}{I_w - I_a}, \tag{10}$$

these expressions can be inverted to obtain:

$$S_w = \frac{\ln\left(\tilde{I} \left[\left(\tau_{sw}/\tau_{sa} \right)^{2k} - 1 \right] + 1 \right)}{2k \ln(\tau_{sw}/\tau_{sa})} \tag{11}$$

which is the Tidwell and Glass (1994) model. The normalized intensity $\tilde{I}$ consists entirely of measured quantities, while the parameter k is formally the number of pores across the system but is taken to be a fitting parameter. By measuring the average light intensity across all pixels covering our flow cell and fitting to the measured amount of water in the cell, we find that $k = 26$ fits the data best (Fig. 2), which is larger, as expected, than a simple face-centered cubic estimate given by $k \approx 13$ mm $/ d_{50} = 18$. Fig. 2 also shows that the volume measurement

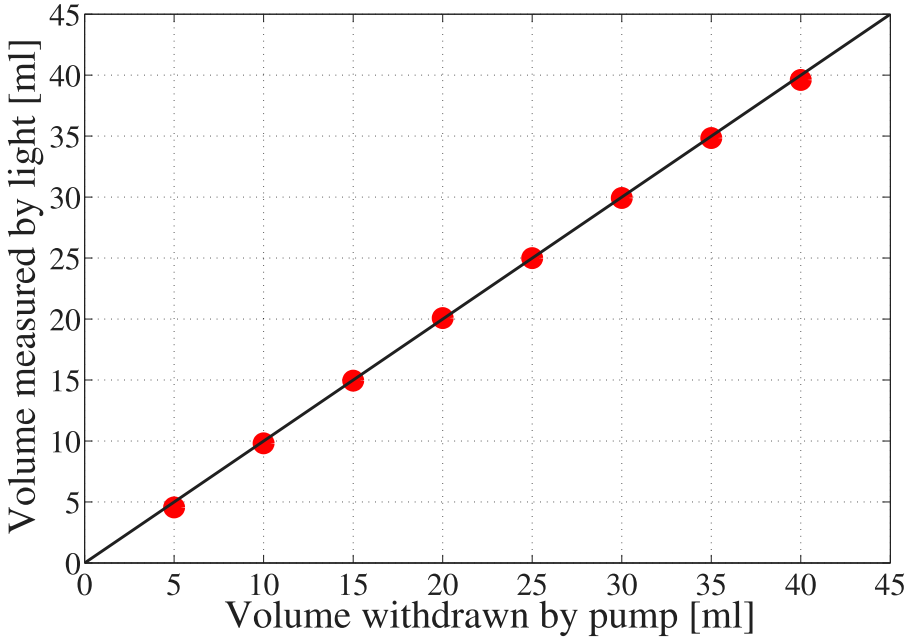

Fig. 2. The volume of water in the cell as measured by light transmission is compared to the volume withdrawn by a syringe pump. The red dots are calculated by summation over 2D saturation images (the black line is 1:1, for reference, and uncertainties are smaller than the symbol size).

is repeatable in 5 ml increments and that accuracy is not affected by the position of the drainage front in the flow cell.

Formally, the *Tidwell and Glass* model of Eq. (11) corresponds to taking the actual distribution of solid, air and water within the cell and redistributing these phases into $k_a = (1 - S_w)k$ layers of air embedded between layers of solid and $k_w = S_w k$ layers of water embedded between solid. This planar model for converting measurements of light intensity at a pixel into measures of water saturation across the width of the cell behind that pixel is clearly an approximation. The model will get worse as pixel size decreases relative to the size of the solid grains. For a face-centered cubic model, some light rays would pass nearly entirely through solid and others almost entirely through pores. The *Tidwell and Glass* model could not be expected to apply until enough transmitted rays passing through all combinations of solid, air and water are recorded on a rectangular patch of the cell. For our random packings, we will have all such rays represented on patches that are a few times larger than the average grain diameter. For our later purposes of comparing measurements to simulations, we measure saturation $s(z)$ as a function of height z in the cell by averaging the light intensity over rectangular patches that are one camera pixel high ($d_{\text{cam}} = 0.59$ mm) at finest resolution and have widths given by $d_{\text{width}} = 56$ mm wide. Even on such rectangular pixels at finest vertical resolution, all ray paths through the solid, air and water will be represented, and Eq. (11) is expected to apply. Because Eq. (11) is a nonlinear relation between $\tilde{I}$ and S_w, whenever a different patch size is used to determine saturation, one should in principle calculate the average values of all of I_a, I_w and I over the new patch size and then calculate the saturation behind the patch using Eqs. (10) and (11). Considering this, we performed saturation measurements at different resolutions both in this manner and by directly averaging the $s(z)$ function obtained first at camera resolution (i.e., on rectangular patches $d_{\text{cam}} \times d_{\text{width}}$), and the results are not significantly different.

2.2. Standard-model numerical simulations

We test the standard model of drainage (Eqs. (1)–(4)) by performing 1D isothermal numerical simulations down the length of our homogeneous cell using the TOUGH2, EOS3 code (Pruess, 2004) and comparing these results to experimental observations.

To accomplish this, the capillary pressure curve used in the TOUGH2 simulations is first determined experimentally under static (non-flowing) equilibrium conditions. Water is drained from the cell slowly (controlled by an external reservoir), until most of it has been invaded from above by air, and the equilibrium water saturation profile $S_w(z)$ is measured optically when the cell reaches steady-state. Fig. 3 shows the height above the phreatic surface versus the static equilibrium water saturation $S_w(z)$ as measured on rectangular patches of size $d_{\text{cam}} \times d_{\text{width}}$. We fit this observation using the van Genuchten model

$$P_n - P_w = P_0(\tilde{S}^{-1/\lambda} - 1)^{1-\lambda} \tag{12}$$

where $\tilde{S}$ is the saturation normalized by residual saturation S_{wc} such that

$$\tilde{S} = \frac{S_w - S_{wc}}{1 - S_{wc}} \tag{13}$$

and where λ and P_0 are fit parameters (note that λ is written as m in van Genuchten's notation). To convert $P_n - P_w$ into height z relative to the air entry point, we use the static equilibrium result that

$$P_n - P_w = \frac{4\gamma \cos\theta}{a_0} + (\rho_w - \rho_a)gz \tag{14}$$

where γ is the air–water surface tension, a_0 is the entry pore diameter (uniform from top to bottom in the cell), θ is the equilibrium contact angle and $4\gamma\cos\theta/a_0$ is the entry pressure into an effective capillary tube of diameter a_0. Equating Eqs. (12) and (14) and using Eq. (13) gives a model for hydrostatic $S_w(z)$ that is shown as the red curve in Fig. 3, with parameter values $\lambda = 0.94$ and $P_0 = 1100$ Pa. The fit is slightly inaccurate as residual saturation is approached higher in the cell. If H is the height of the cell, we expect that residual saturation will occur at a height $z = h < H$, where h scales with Bo and Ca, and that the capillary pressure will be a finite constant $4\gamma\cos\theta/a_0 + (\rho_w - \rho_a)gh$ for all points $z > h$. In Fig. 3, $h \approx 8$ cm. The observed entry pressure of 863 Pa indicates an equilibrium contact angle of approximately 45 degrees, which we use throughout.

The relative permeability of water is given by the van Genuchten–Mualem model, which uses the same λ as the capillary pressure curve

$$\kappa_w = \begin{cases} \sqrt{\tilde{S}}[1 - (1 - [\tilde{S}]^{1/\lambda})^{\lambda}]^2 & \text{for } 0 \le \tilde{S} \le 1 \\ 0 & \text{for } \tilde{S} < 0. \end{cases} \tag{15}$$

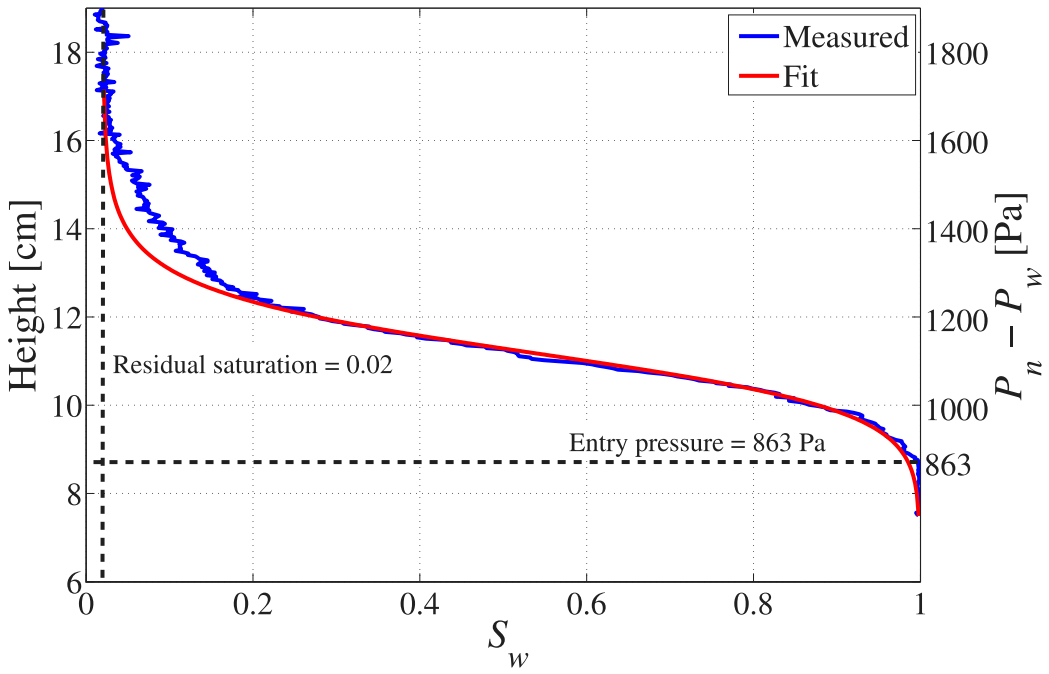

Fig. 3. A steady-state saturation profile is measured optically (blue) as a function of height above the phreatic surface. The van Genuchten model (Eq. (12) with $\lambda = 0.94$ and $P_0 = 1100$ Pa) is fit to the observations, and we observe a residual water saturation of $S_{wc} = 0.02$. Note that the air entry pressure marked on the graph is not equivalent to the variable P_0.

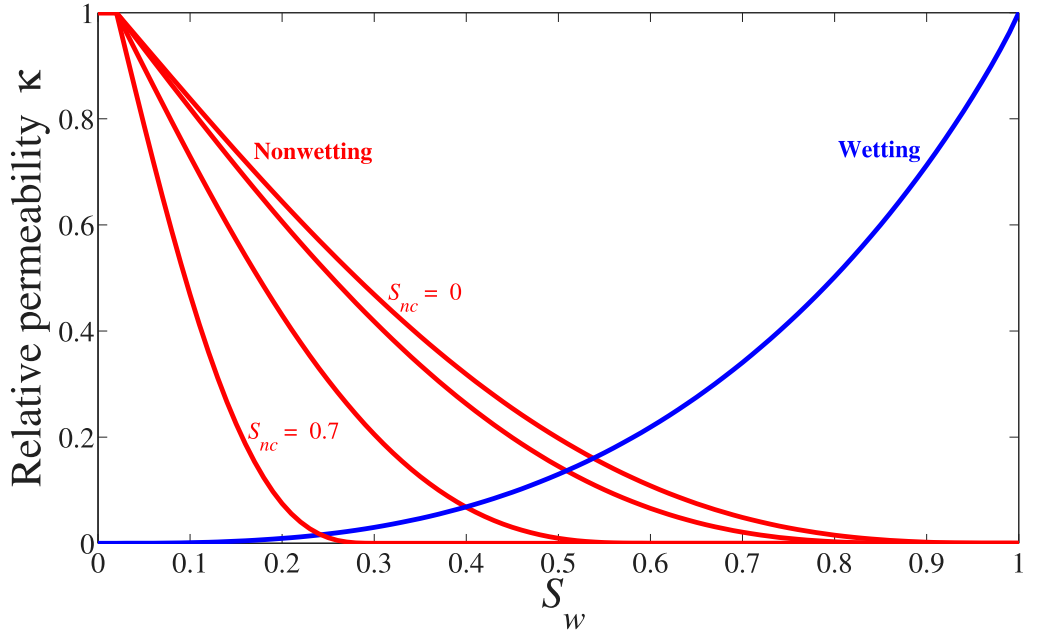

Fig. 4. The relative permeability curves used in the numerical simulations are plotted. For the gas phase, we use the Corey model with a range of values for S_{nc}. For the water phase, we use the van Genuchten model with parameters taken from the fit to the static saturation profile.

The water's relative permeability has no free fit parameters (residual saturation S_{wc} is experimentally observed), and, conceptually, water is not allowed to flow if $S_w \leq S_{wc}$. In contrast, we use a Corey relative permeability curve for the air

$$\kappa_n = \begin{cases} (1-\hat{S})^2(1-\hat{S}^2) & \text{for } \hat{S} \leq 1 \\ 0 & \text{for } \hat{S} > 1 \end{cases} \tag{16}$$

where

$$\hat{S} = \frac{S_w - S_{wc}}{1 - S_{nc} - S_{wc}}. \tag{17}$$

Water saturation in the range $1 - S_{nc} \leq S_w \leq 1$ corresponds to $\hat{S} > 1$, which requires $\kappa_n = 0$. This model for κ_n allows us to vary S_{nc} from $S_{nc} = 0$ to $S_{nc} = 0.9$ in the simulations. Fig. 4 shows some of the corresponding relative permeability curves.

Finally, the initial condition for the simulations is full static water saturation. The upper boundary is maintained at atmospheric pressure (air pressure is approximately atmospheric throughout the cell), and the lower boundary has a constant water flux as imposed by the syringe pump. Because the side boundaries of the actual 3D cell have zero lateral flux conditions, the entire cell is reasonably modeled as a 1D,

cell-length system. The discretization for the 1D simulations is a stack of identical 10 mm tall voxels, fifteen in all, implicitly having the same width and depth as the cell, with two boundary voxels at the top and bottom.

2.3. Comparing experiments to standard-model simulations

Fig. 5 shows snapshots during drainage when gas begins to invade the bottom voxel of the field of study. The plotted comparisons are between the TOUGH2 simulations, the optically-measured saturation fields at the highest and lowest Ca, and hydrostatic conditions. Red horizontal lines denote the averaging voxels in the flow cell, which are also the simulation voxels. The gray images of optically determined saturation were determined on square pixels of size $d_{\text{cam}} \times d_{\text{cam}}$. The black dots marked "cell" in the graphs are the saturations optically determined by averaging light intensity over the rectangular patches that correspond to the simulation voxels (the red lines of size 10 mm $\times d_{\text{width}}$). The red dots marked "simulation" are the standard model simulation results. First gas invasion occurs in the simulations when gas starts flowing out of the upstream voxel. The black line in the graphs are the optically-measured hydrostatic saturations, which are equivalent to Fig. 3 but measured on patches of size $d_{\text{cam}} \times d_{\text{width}}$ resolution. The black round circles are the optically-measured hydrostatic saturations on the simulation voxels (10 mm $\times d_{\text{width}}$).

The simulations (red dots) were performed using a van Genuchten model for $P_c(S_w)$ and $\kappa_w(S_w)$ that was fit to the measured equilibrium hydrostatic saturation profile according to standard practice. We observe that for our voxel size $L_z = 10$ mm, the average S_{nc} is approximately 0.08 at Ca $= 5.0 \times 10^{-5}$ and 0.04 at Ca $= 1.5 \times 10^{-3}$. The fact that all parameters in the standard-model simulations were measured independently prior to the gas-invasion experiments and yet there remain significant differences between the simulation and optical measurements of saturation indicates that inappropriate assumptions are present in the standard model.

Fig. 6 demonstrates how the parameter S_{nc} influences the air breakthrough time (i.e., the time for air to traverse the length of the field of study from the first Haines jump at the top to the final Haines jump that allows air to first touch the bottom boundary). In these simulations, we used the same S_{nc} for each of the 15 numerical voxels. Perhaps the most significant aspect of these results is that if $S_{nc} = 0$ for the gas phase, the simulated breakthrough time is 3.7 times faster than the observed breakthrough time. The simulated breakthrough times are influenced both by the capillary pressure function and the relative permeability functions for each phase. The general trend that increasing S_{nc} slows down simulated breakthrough times is expected because higher S_{nc} requires more air to enter each voxel before desaturating the next one downstream. However, the result that the best S_{nc} for predicting breakthrough times at Ca $= 1.5 \times 10^{-3}$ is roughly 0.72, while the optically measured S_{nc} at this capillary number and voxel size is 0.08, may be a result of using the improper equilibrium $P_c(S_w)$ relation at high capillary number, as well as the fact that the van Genuchten (1980) model for $P_c(S_w)$ is problematic in the range of $1 - S_{nc} < S_w < 1$. How rapidly an individual simulation voxel achieves S_{nc} is strongly influenced both by the $P_c(S_w)$ function for that voxel in the range $1 - S_{nc} < S_w < 1$ and by the influence of the relative permeability model on pressure gradients.

The main conclusion of the present section, in which laboratory measurements of saturation in a flow cell have been compared to numerical simulations based on the standard model of two-phase flow with all free parameters independently measured, is that the standard model does not adequately reproduce the experimentally observed drainage profiles. Two key features are missing from the standard model: (1) rules for how S_w varies in each voxel as it is being invaded for the first time, based on the physics of gravity-stabilized drainage; and (2) once a voxel percolates with gas at $S_w \leq 1 - S_{nc}$, new models for $P_c(S_w)$, $\kappa_w(S_w)$ and $\kappa_n(S_w)$ must be used, with dependence on Ca, as first illustrated in Fig. 5, and with dependencies on Bo and L_z as demonstrated in the following sections. Overall, the standard model can only apply to voxels where both fluid phases percolate and does not address the actual capillary physics and associated saturation structures occurring in those voxels that are being actively invaded for the first time.

3. Saturation models for stable invasion

To incorporate Bo and Ca into models for S_{nc} and, more broadly, into models for how saturation varies behind the invasion front, we turn to percolation theory. Most of our analysis will be motivated by the Wilkinson (1984) Invasion Percolation (IP) algorithm in the presence of a buoyancy force and finite viscous flow. Our first goal is to obtain models for how nonwetting saturation varies with distance behind the front, which will allow us to determine the dependencies within a $S_{nc}(\text{Bo}, \text{Ca}, L_z)$ function.

In what follows, we will not rederive all needed IP scaling results from the literature but will attempt to describe in words the physics involved. Further, several of the scalings have exponents that we take from numerical simulations of IP, and the models that follow are therefore not built entirely from theoretical analysis and are meant only to capture the scalings and trends observed in the laboratory measurements and IP numerical simulations.

3.1. Saturation model when Bo = 0 and Ca ≈ 0

Consider first that gravity is not present and that the invading fluid is moving slowly enough for the Invasion Percolation algorithm of Wilkinson and Willemsen (1983) to be valid. The condition for Invasion Percolation to be a realistic model is that the viscosity-controlled pressure drop across a voxel of length L_z is small compared to the capillary pressure drop across a meniscus residing in an entry pore of radius a_0, which corresponds to the condition that $\text{Ca} \ll a_0/L_z$.

If the voxel has lengths L_x and L_y (both $> L_z$) in the lateral directions, we divide the voxel into cubes of volume L_z^3, so that there will be $L_x L_y L_z / L_z^3 = L_x L_y / L_z^2$ such cubes in the voxel. In this case, the critical volume of injected fluid at percolation within a large invasion cluster is a fractal given by Wilkinson and Willemsen (1983)

$$V_{nc}^{\infty} = \phi a_0^3 \left(\frac{L_z}{a_0}\right)^{D_c} \frac{L_x L_y}{L_z^2} \tag{18}$$

where ϕ is the porosity of the material, and D_c is the fractal dimension for ordinary capillary fingering without the influence of pressure gradients, which in a 3D cubic lattice has the universal value $D_c = 2.52$ (and $D_c = 91/48 = 1.90$ in 2D). This result holds for the infinite cluster that is sampled in sufficiently large systems, as denoted by the superscript ∞. The subscript n again denotes nonwetting, while subscript c denotes the critical threshold at percolation.

The saturation associated with the invaded volume V_{nc}^{∞} is found by dividing by the total pore volume $\phi L_x L_y L_z$

$$S_{nc}^{\infty} = \frac{V_{nc}^{\infty}}{\phi L_x L_y L_z} = \left(\frac{L_z}{a_0}\right)^{(D_c - d)} \tag{19}$$

where d is the Euclidean-space dimension of the system. Because $D_c - d$ is negative, the saturation of invading nonwetting fluid at breakthrough is a decreasing function of the size of the voxel in the direction of flow. Note that if the smallest system (voxel) dimension was L_x and not L_z, then the above argument would repeat by paving the saturation structure with cubes of volume L_x^d, resulting in $S_{nc}^{\infty} = (L_x/a_0)^{D_c - d}$.

Such slow invasion when Bo $= 0$ can begin to occur once the applied capillary pressure $P_c = P_n - P_w$ exceeds a threshold given by $P_c \geq \gamma/a_0$. From the macroscopic porous-continuum perspective, in which the fluid pressure fluctuations due to Haines jumps are not detected, as long as each voxel has the same a_0, the slow invasion will proceed with P_c uniform and with both fluids percolating across all

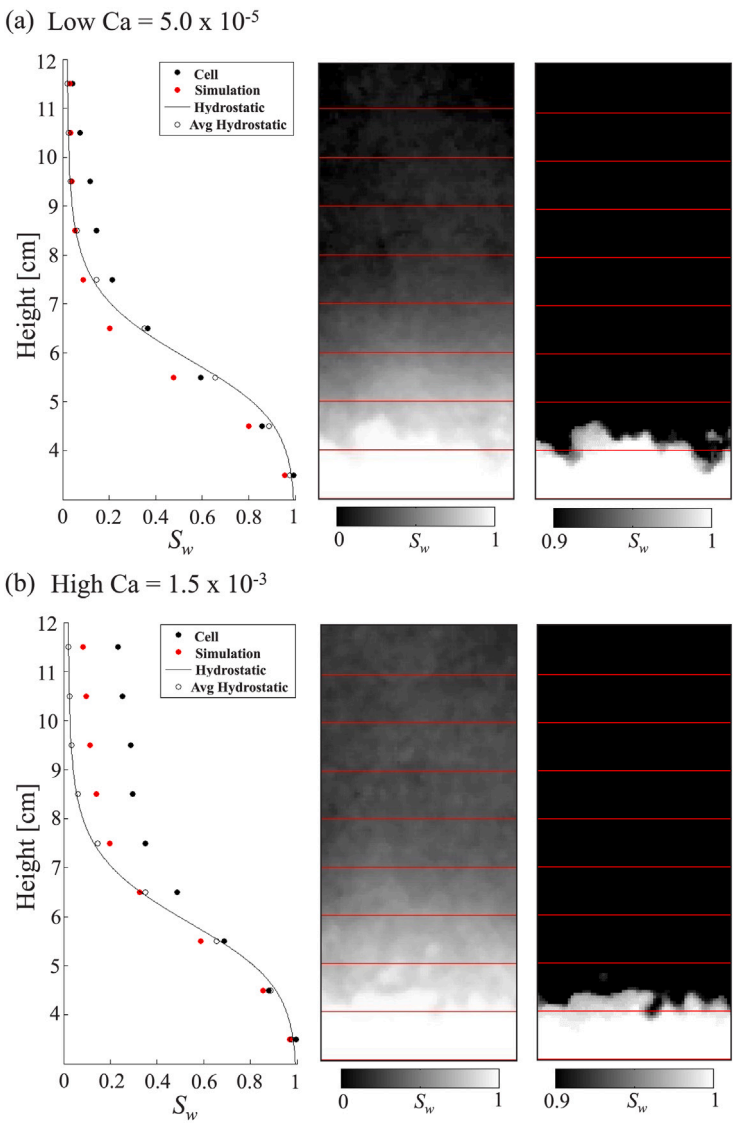

Fig. 5. S_w observations from experiments at low (a) and high (b) Ca are shown. The 2D S_w images at center and right use different grayscale thresholds to highlight upstream and frontal regions, respectively. On the left, saturation is scaled up to the voxel size (red circles on the 2D S_w images) and plotted alongside simulations. Height on the vertical axis is relative to the bottom of the cell. Uncertainties are smaller than the symbol size. Hydrostatic S_w curves from Fig. 3 are included to show how S_w distorts during flow (i.e. at nonzero Ca). The saturation plots on the left are vertically aligned with the 2D S_w images.

invaded voxels. To view the emergent nonwetting saturation profile $s(z)$ for invasion occurring in the $-z$ direction (with $z = 0$ defining the tip of the invasion cluster), we use the fast Invasion Percolation algorithm of Masson (2016) which allows for trapping. Simulation is performed on a 3D system of size $N_x = 400$, $N_y = 400$, and $N_z = 1600$ that has periodic boundary conditions in the x and y direction with injection occurring from all points of the face $z = N_z$. For this scenario, the limiting (maximum) saturation along $s(z)$ associated with the infinite cluster is given by $S_{nc}^{\infty} = N_x^{D_c - d} = (400)^{-0.48} = 0.06$, which holds for large enough z.

In Fig. 7 we plot the saturation profile $s(z)$ obtained using the IP simulation as well as the expression

$$s(z) = S_{nc}^{\infty} \frac{(z/w_o)^{\epsilon_1 \epsilon_2}}{[1 + (z/w_o)^{\epsilon_1}]^{\epsilon_2}} \tag{20}$$

with fit parameters $w_o = 122$, $\epsilon_1 = 1.2$, and $\epsilon_2 = 2.1$. This form is purely empirical and was chosen to match the sigmoidal shape that tends to the constant theoretical value of $s_{nc}^{\infty} = N_x^{D_c - d}$ after passing through the inflection at $z = w$, where w is measured to be $w = 89.7$ for the given fit parameters. The saturation at the inflection point s_w is thus

$$s_w = f_w S_{nc}^{\infty} \tag{21}$$

where the parameter f_w is defined

$$f_w = \frac{(w/w_o)^{\epsilon_1 \epsilon_2}}{[1 + (w/w_o)^{\epsilon_1}]^{\epsilon_2}} \tag{22}$$

where $w/w_o \approx 0.74$ and $f_w \approx 0.15$.

In a finite system of size L_z, the saturation of nonwetting fluid at percolation is

$$S_{nc} = \frac{1}{L_z} \int_0^{L_z} s(z)\, dz. \tag{23}$$

We then have $\lim_{L_z \to \infty} S_{nc} \to S_{nc}^{\infty}$ in a sufficiently large system where the saturation near the injection boundary and the fall off in saturation toward the invasion tip do not occupy a significant fraction of the total system volume.

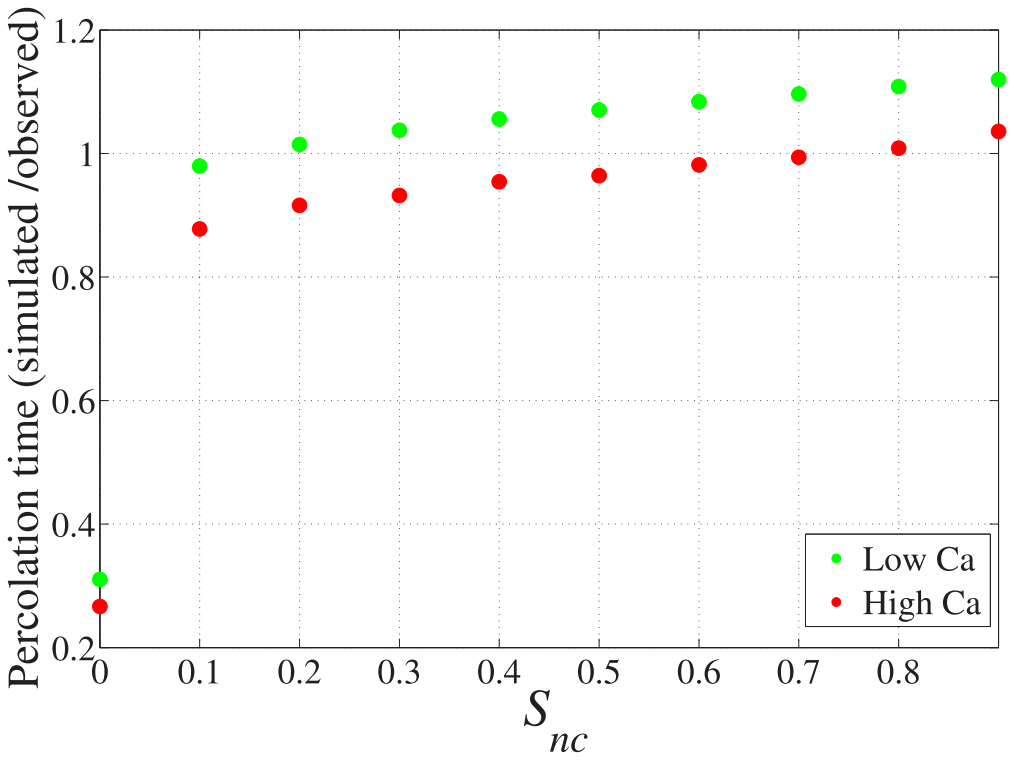

Fig. 6. Percolation times indicate that finite values of S_{nc} can cause approximately fifteen percent variability in front speed, while $S_{nc} = 0$ allows a thin finger of air to propagate very quickly. To match observed front speed, artificially high and Ca-dependent S_{nc} values are needed.

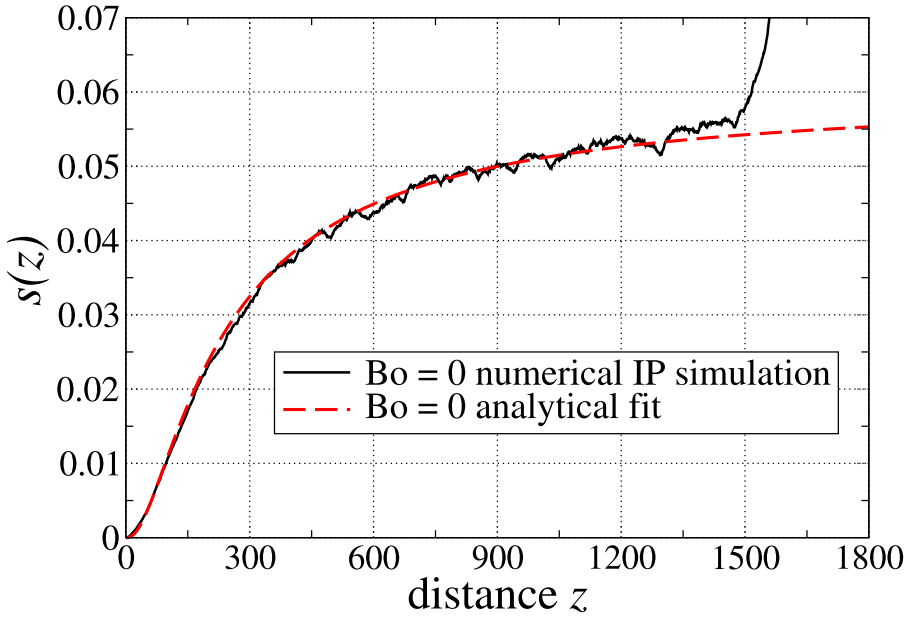

Fig. 7. IP simulation at Bo = 0 of the nonwetting saturation profile $s(z)$ of an IP invasion cluster at breakthrough with $z = 0$ at the tip, and the injection face at $z = 1600$. Total system size was 400 × 400 × 1600. The saturation state is perturbed by the injection boundary for a distance of roughly 100 lattice points. The dashed curve is the function of Eq. (20).

3.2. *Saturation model when* Bo > 0 *and* Ca ≈ 0

Wilkinson (1984) defines a variant of Invasion Percolation that incorporates variable P_c due to gravity (IP in a gradient field) when the invasion is again occurring so slowly that viscosity may be neglected.

If Bo is positive (e.g., air invading water in the direction of gravity), the invasion front is stabilized; i.e., long fingers of invading fluid do not develop and, further, the region over which both phases percolate behind the front becomes compressed compared to when gravity does not act. For a gas invading a liquid (drainage) with Bo > 0, downward gas jumps in the direction of gravity are somewhat less favored due to the increasing liquid pressure compared to horizontal jumps, with the result that trapped clusters of defending fluid develop even in 3D. However, if Bo < 0 (e.g., air invading water against the gravity field), unstable gravitational fingers develop because upward gas jumps

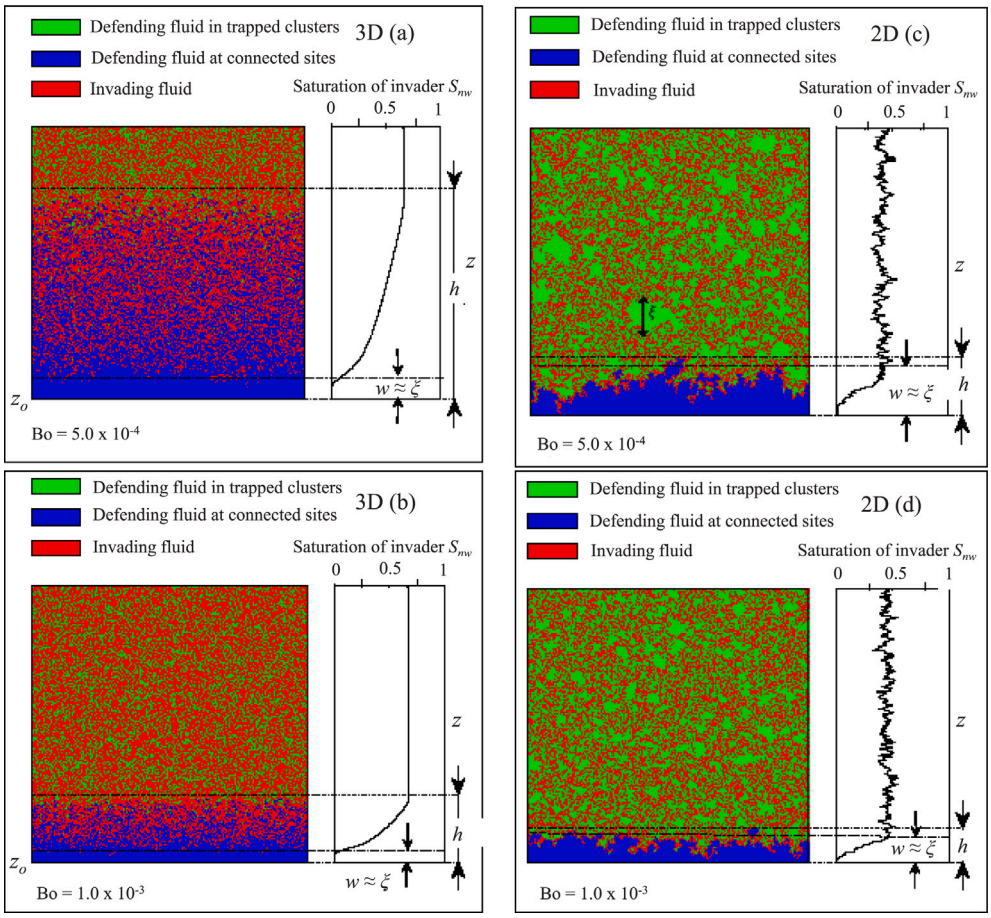

Fig. 8. Snapshots of IP numerical results both in 3D (column on left) and 2D (column on right) at the moment of percolation. In 3D, each vertical slice is through the middle of the 400 × 400 × 400 system. In all panels, the red fluid invades from the top surface to the bottom. The length h between the front tip and the point where the defending fluid is entirely disconnected into isolated clusters is measured numerically on the entire 3D system, not just on the slices shown in (a) and (b). The front width w was measured numerically as the inflection point in the saturation profile and corresponds to the scaling of Eq. (28). The maximum trapped cluster size is the same as the front width ($\xi = w$) when viscous pressure gradients can be neglected. In 3D, the lengths $\xi = w$ and h are distinct and have different scalings with Bo, while in 2D we observe $\xi = w \approx h$. Also, in 3D the residual saturation of the defending phase is much lower than in 2D, and ξ is smaller.

are favored relative to horizontal jumps due to the decreasing liquid pressure with upward distance.

For stable gas invasion in the direction of gravity, the Wilkinson (1984) model of IP results in a transition layer of thickness h behind the lead menisci (which we continue to define as being located at $z = 0$) that separates the capillary fingering occurring in the frontal region from a constant, statistically homogeneous "residual saturation" region well behind the front. Across the region $0 < z < h$ behind the front, in 3D, both phases form connected paths. Above this region (i.e., $z > h$), the liquid is below the percolation threshold, the capillary pressure is at a maximum, and all parts of the pore space originally occupied by liquid that can be invaded by gas have already been invaded. Any remaining liquid is in disconnected clusters of maximum size ξ that corresponds to the correlation length in the defending liquid. As gas flows through this residual-saturation region to get to the advancing menisci at the front, no further jumps or changes to the saturation state occur. The liquid does not flow in the residual-saturation region. In addition, near the front where the gas phase first percolates at $z = 0$, we can define a second correlation length w within the gas phase that effectively defines the width of the random capillary-fingering region occurring immediately behind the front.

At the position of the lead miniscii ($z = 0$) there are capillary fingers probing the porous material for the smallest capillary pressure threshold to invade next. This random capillary-fingering structure immediately behind the lead menisci ($0 \le z \le w$) transitions after an inflection point at $z = w$ into the region ($w \le z \le h$) where the increasing capillary pressure with increasing z is causing defending fluid to become pinched off in places until for distances $z > h$ the defending fluid is entirely disconnected into patches having maximum size ξ.

The three lengths w, ξ and h can be viewed in the numerical snapshots of the saturation distribution shown in Fig. 8. These were made with the Invasion Percolation algorithm of Masson (2016) on a 400 × 400 × 400 point grid in 3D and 400 × 400 in 2D. The simulations are of a lighter fluid like air slowly invading downward (in the direction of gravity) into a denser defending fluid like water. In 2D, all three lengths are equivalent $w \approx \xi \approx h$, while in 3D with a uniform gravitational pressure gradient, we have $w \approx \xi < h$. When variable viscous pressure gradients are present, as considered later, in 3D we will have $w < \xi < h$. Note that the definition of front width, w, in 3D is the inflection point of the $s(z)$ curve, while in 2D it is the maximum separation distance in z of the lead menisci.

A major goal of this work is to obtain an expression for the invading-fluid saturation profile $s(z)$. There are five key observables that scale with Bo and serve as anchor values for the $s(z)$ profiles. These are: (1) the width w(Bo) of the capillary-fingering region immediately behind the front; (2) the invading fluid's saturation s_w(Bo) at $z = w$; (3) the slope of the saturation profile at $z = w$ defined as b_w(Bo) = $ds(z)/dz|_{z=w}$; (4) the width h(Bo) of the entire dual-percolation zone; and (5) the saturation s_h(Bo) at $z = h$. Additionally, we require that at $z = h$, the slope is zero $ds(z)/dz = 0$, and the curvature is negative $d^2s(z)/dz^2 < 0$. We now go on to obtain the scaling laws for these five

observables and then propose functional forms for the profile $s(z)$ that are anchored by these values.

3.2.1. Observables at the front: w, s_w and b_w

A first step is to establish how the width w of the frontal region scales with Bo. The argument is similar to that for how the maximum length ξ of the residual-water clusters depends on Bo. All of Wilkinson (1984), Rosso et al. (1985), Birovljev et al. (1991), and Méheustt et al. (2002) derive the scaling for ξ, and we follow a similar argument for w here. The width of the front w can be interpreted as a correlation length in the invading gas phase and addressed with ideas from ordinary percolation. Let q be the allowed occupation probability of the invading gas within voxels behind the front. This is formally distinct from the gas saturation because not all pores initially filled with water can be invaded if that water is trapped (i.e., surrounded by gas), while the definition of q allows for all water-filled pores to potentially be invaded by gas if the local capillary pressure exceeds the entry threshold of the water-filled pore. At the lead voxel just behind the front $z = 0$, there is a percolation threshold q_c that occurs at the capillary entry pressure $P_c(z = 0) = \gamma/a_0$ for that voxel. The relation for the occupation probabilities $q(z)$ at a distance z behind the front can be written

$$q(z) - q_c = \int_{P_c(0)}^{P_c(z)} \pi(P)\, dP \tag{24}$$

where $P = \gamma/a$ is the threshold capillary pressure for air to enter a water-saturated pore of size a, and $\pi(P)$ is the probability distribution for these thresholds. If $\pi(P)$ is relatively flat with width $W_t = \gamma(1/a_{\min} - 1/a_{\max})$, we can approximate $\pi(P) \approx 1/W_t$ and write

$$q(z) - q_c = \frac{P_c(z) - P_c(0)}{W_t} = \frac{1}{W_t}\int_0^z \frac{\partial P_c(z')}{\partial z'}\, dz'. \tag{25}$$

We can then define a correlation length w from the usual percolation definition $w \propto [q(w) - q_c]^{-\nu}$ or

$$\frac{w}{a_0} = \text{const}\left(\frac{1}{W_t}\int_0^w \frac{\partial P_c(z')}{\partial z'}\, dz'\right)^{-\nu} \tag{26}$$

$$= \text{const}\left(\frac{a_0}{W_t}\frac{1}{w}\int_0^w \frac{\partial P_c(z')}{\partial z'}\, dz'\right)^{-\nu/(1+\nu)} \tag{27}$$

where $\nu = 0.875$ in 3D (and 4/3 in 2D). We finally rewrite this as

$$w = \ell_w\left(\frac{a_0^2}{\gamma}\frac{1}{w}\int_0^w \frac{\partial P_c(z')}{\partial z'}\, dz'\right)^{-\mu} \tag{28}$$

where $\mu = \nu/(1 + \nu) = 0.47$ in 3D (and 0.57 in 2D), and the pressure-independent length

$$\ell_w = \text{const}\ a_0\left(\frac{a_0 W_t}{\gamma}\right)^{\mu} \tag{29}$$

is adjusted to fit data. The dimensionless quantity $a_0 W_t/\gamma$ only depends on the pore size distribution. Eq. (28) for w is valid even if the capillary pressure gradient is variable behind the front, as it will be at finite wetting-phase velocity.

At small rates of extraction defined by Ca $\ll a_0/L_z$, the capillary pressure gradient is due to gravity alone, which is uniform in space. In this case, Eq. (28) becomes

$$w = \ell_w \text{Bo}^{-\mu}. \tag{30}$$

To test this prediction, we use the fast algorithm of Masson (2016) for Invasion Percolation in a gradient to perform numerical simulations on systems of size $N_x \times N_y \times N_z$. Our flow-cell experiments, when measured in lattice units corresponding to the average distance between two pores, constitute a system size of $N_x = 18$, $N_y = 105$ and $N_z = 212$, which we use in the numerical experiments.

To measure w numerically, we define it as the inflection point in the nonwetting saturation profile $s(z)$. For each Bo, we generate numerically an IP nonwetting saturation curve $s(z)$ at the moment that the nonwetting invading fluid first percolates the system. By taking a derivative $ds(z)/dz$ and identifying $z = w$ as the point where the derivative is maximized, we obtain the front width w for each Bo, as well as the corresponding saturation $s_w = s(w)$ and the maximum slope $b_w = ds(z)/dz|_{z=w}$ at the point $z = w$. The results are plotted in Figs. 9–11.

Fig. 9 shows that although at large Bo there is indeed the predicted power-law relation of $w = \ell_w \text{Bo}^{-\mu}$ with $\mu = 0.47$ (3D), there is a transition to the constant w_0 for Bo $\le$ Bo$_t$. The model fit given in Fig. 9 is given by

$$w = w_0 + \frac{\ell_w \text{Bo}^{-\mu} - w_0}{1 + (\text{Bo}/\text{Bo}_t)^{-2}}. \tag{31}$$

Taking $a_0 = 1$ and $L_x = 18$ for the IP simulations, we have $w_0 = 18^{0.81} = 10.4$ (lattice units). The two free fit parameters that are set to the IP-generated observations of w(Bo) are $\ell_w = 0.7$ (lattice units) and $\text{Bo}_t = 2 \times 10^{-4}$.

For the saturation s_w measured numerically at $z = w$, Fig. 10 again shows a power law at large Bo transitioning for Bo $<$ Bo$_t$ to the constant s_{w0}. The exponent of the power law can be explained by recognizing that across $0 \le z \le w$, there are random capillary fingers that have a saturation that scale as in regular IP, $(w/a_0)^{D_c - d}$, such that $s_w = c_{sw}\text{Bo}^{\beta_w}$, where the exponent is

$$\beta_w = \mu(d - D_c) \tag{32}$$

or $\beta_w = 0.22$ in 3D. This is precisely the slope seen in Fig. 10. Allowing for the transition at Bo$_t$ to constant s_{w0} at low Bond number, the model fit is then given by

$$s_w = s_{w0} + \frac{c_{sw}\text{Bo}^{\beta_w} - s_{w0}}{1 + (\text{Bo}/\text{Bo}_t)^{-2}}. \tag{33}$$

The two free parameters that are set to the IP simulations of s_w(Bo) are $s_{w0} = 0.02$ and $c_{sw} = 0.63$.

Last, the maximum slope b_w(Bo) of the $s(z)$ curve at the inflection point $z = w$ is given in Fig. 11. The model fit is given by

$$b_w = b_{w0} + \frac{c_{bw}\text{Bo}^{\omega} - b_{w0}}{1 + (\text{Bo}/\text{Bo}_t)^{-2}} \tag{34}$$

where the exponent is observed to be $\omega = 0.64$ and $b_{w0} = 2.6 \times 10^{-3}$ (inverse lattice units) and $c_{bw} = 1.06$.

3.2.2. Observables at the residual-saturation transition: ξ, h and s_h

For the maximum size ξ of residual water clusters above $z = h$, we use an identical correlation length argument as was used for w and used by Méheustt et al. (2002) and others. However, this time we are focusing on the occupation probabilities $p = 1 - q$ of the water phase and considering the correlation length of the water clusters near percolation of the water phase p_c that takes place in the region $z \ge h$, corresponding to the residual water saturation S_{wc} with capillary pressure $P_c(h)$. We find the following expression,

$$\xi = \ell_\xi\left(\frac{a_0^2}{\gamma}\frac{1}{\xi}\int_{h-\xi}^{h} \frac{\partial P_c(z')}{\partial z'}\, dz'\right)^{-\mu} \tag{35}$$

where the length ℓ_ξ is adjusted to fit data. When capillary pressure gradients are variable behind the front due to finite viscous flow, ξ and w are distinct lengths because they involve distinct capillary pressure drops with $w \le \xi$.

For the case of gravity acting alone at small rates of extraction, $\partial P_c(z)/\partial z = \Delta\rho g$ is a constant (note that gravity is directed in the opposite direction to increasing z) such that $w = \xi$. Using the definition of Bo then yields

$$\xi = w = \ell_\xi \text{Bo}^{-\mu} \tag{36}$$

which Birovljev et al. (1991) found to fit their 2D measurements on flow through a layer of beads in a Hele–Shaw cell with $\mu = 0.57$, as predicted in 2D.

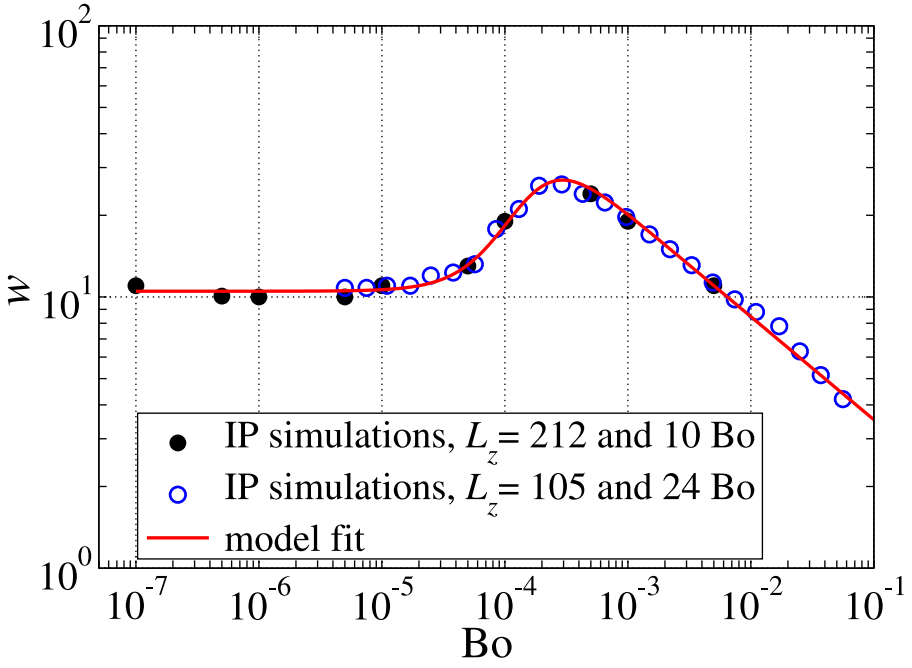

Fig. 9. Numerical measurements of the inflection point w as a function of Bo (measured in lattice units using the fast IP algorithm of Masson (2016) that does not invade trapped clusters). The model fit corresponds to Eq. (31). The simulation domain has dimensions (measured in lattice units) of $18 \times 105 \times L_z$. Two different L_z were considered: $L_z = 212$ (with 10 different Bo) and $L_z = 105$ (with 24 different Bo).

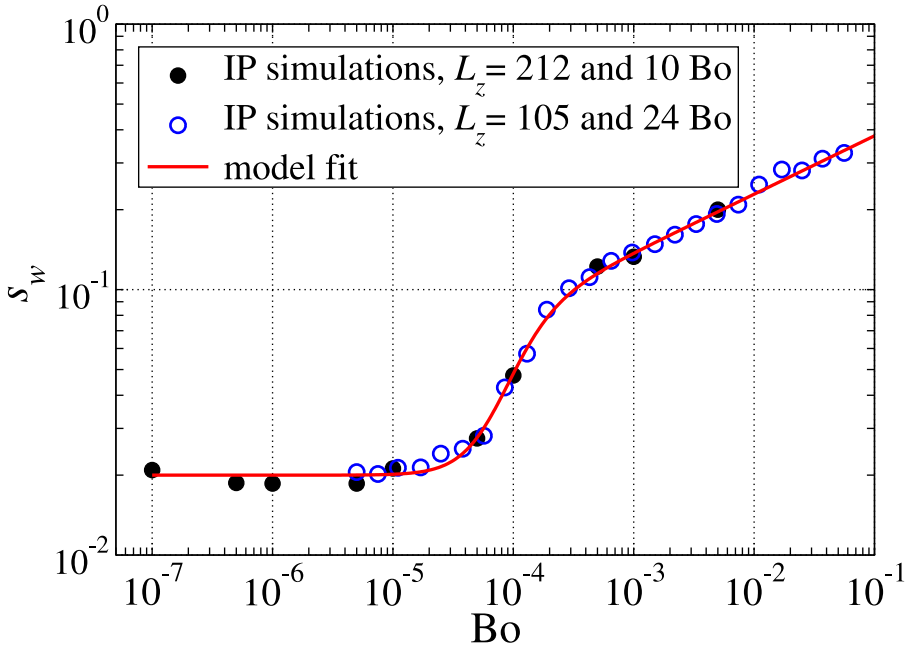

Fig. 10. Numerical measurements of the invading saturation s_w defined at the point $z = w$ as a function of Bo. The model fit corresponds to Eq. (33).

Wilkinson (1984) defines the transition length h by considering the capillary pressure drop across the distance h to obtain $\gamma/a_h - \gamma/a_0 = \Delta\rho g h$, where $a_h < a_0$ is the smaller pore size being invaded by air at $z = h$. At $z = h$, the capillary pressure is larger compared to at $z = 0$ by an amount $\Delta\rho g h$. This can be stated

$$\frac{h}{a_0} = \frac{a_0/a_h - 1}{\mathrm{Bo}}. \tag{37}$$

To test the Wilkinson (1984) prediction of $h \propto \mathrm{Bo}^{-1}$, we use the fast algorithm of Masson (2016) and perform numerical IP experiments in a uniform gravity field when trapped clusters of defending fluid are not allowed to be invaded. For simulations conducted on a $400 \times 400 \times 400$ cubic lattice in 3D (and a 400×400 square lattice in 2D) with periodic boundary conditions in the directions lateral to average flow, we observe a different scaling for h, as shown in Fig. 12, with $h \propto \mathrm{Bo}^{-0.85}$ (exponent $\neq -1$).

Given these IP simulations, we propose that the length h will satisfy a scaling of similar form to w and ξ, but with a different exponent μ_h; i.e., h should depend on the difference in the capillary pressure across the dual percolation region so that

$$h = \ell_h \left(\frac{a_0^2}{\gamma} \frac{1}{h} \int_0^h \frac{\partial P_c(z')}{\partial z'} \, dz' \right)^{-\mu_h} \tag{38}$$

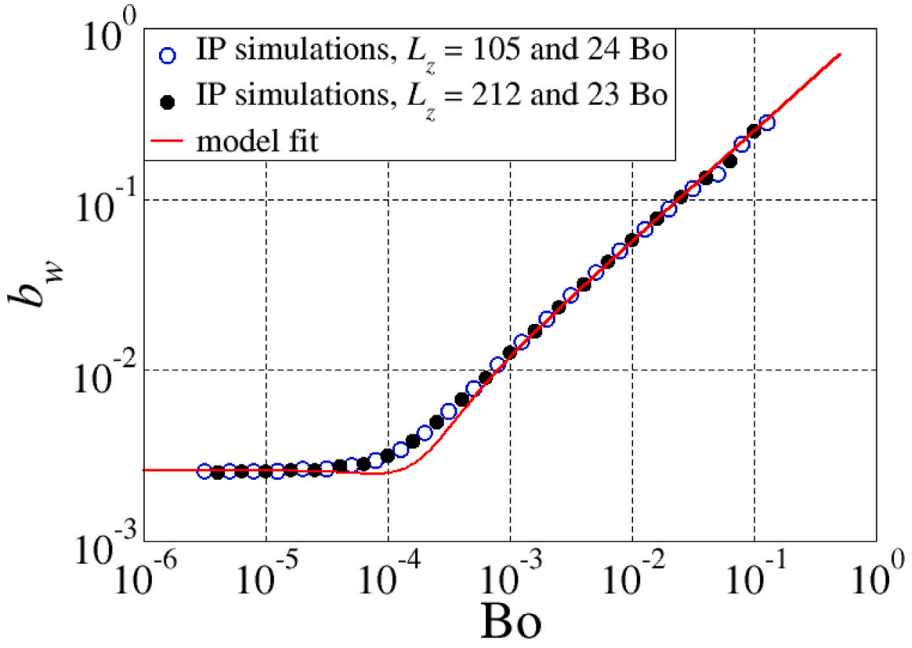

Fig. 11. Numerical measurements of the slope $b_w = ds(z)/dz|_{z=w}$ of the saturation profile at the point $z = w$. The model fit corresponds to Eq. (34).

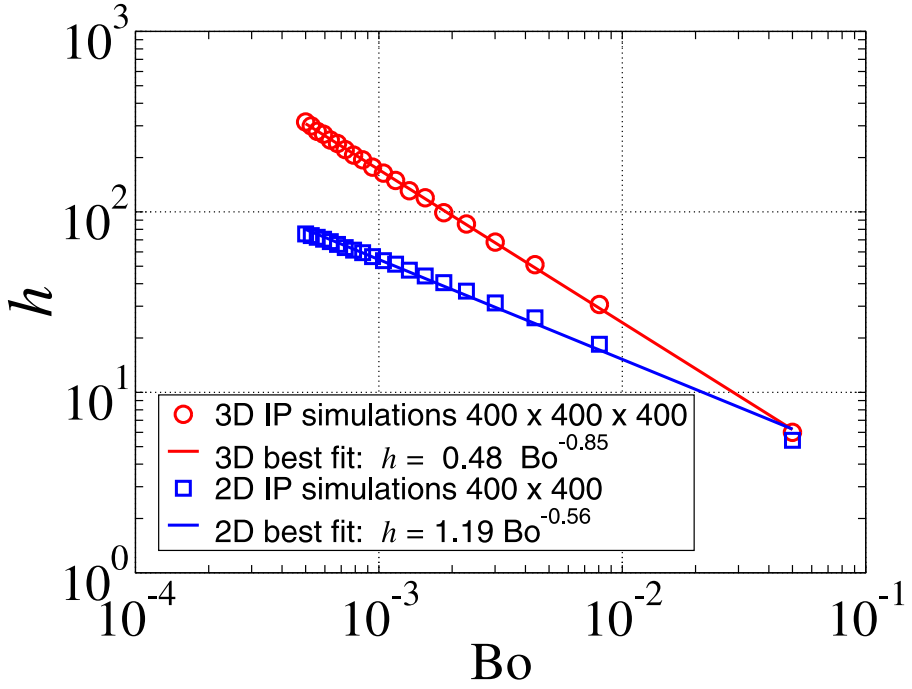

Fig. 12. Numerical measurements in 2D and 3D of the dual-percolation length h (measured in lattice units) using the fast IP algorithm of Masson (2016) with periodic boundary conditions in the directions lateral to average flow.

where ℓ_h is a pressure-independent length that must be adjusted to fit data. For the case of gravity alone, we then have

$$h = \ell_h \mathrm{Bo}^{-\mu_h} \tag{39}$$

As shown in Fig. 12, we numerically measure h in both 2D and 3D and observe the scalings

$$h = \begin{cases} 0.48\mathrm{Bo}^{-0.85} & \text{in 3D} \\ 1.19\mathrm{Bo}^{-0.56} \approx \xi & \text{in 2D} \end{cases} \tag{40}$$

In 2D, we observe numerically that $h \approx \xi$. Once the size of the "fjords" of defending fluid, which extend from the front region into the invaded region, become comparable to the correlation length ξ, they are pinched off. This results in the defending fluid becoming completely disconnected at distances ξ or greater behind the front, with the result that $w = \xi \approx h$.

In 3D, the additional spatial degree of freedom for the defending fluid allows the fjords to remain continuous into the invaded region even when the entrance to a fjord becomes pinched off in places. Only at a distance $h > \xi$ will a fjord finally become completely closed off in all three space dimensions, and that distance h will increase with the decreasing influence of gravity. In the absence of gravity in 3D, the fjords are never entirely cut off, $h \to \infty$, and the residual saturation of the defending fluid is close to zero, while the saturation of the invading

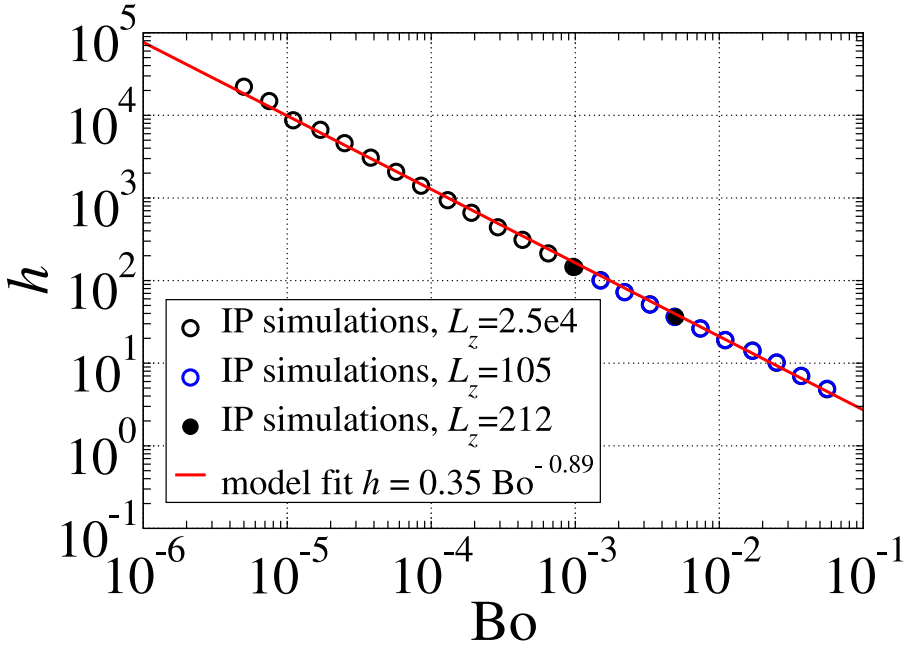

Fig. 13. Numerical measurements of the dual-percolation length h measured in lattice units using the fast IP algorithm of Masson (2016) on systems of size $18 \times 105 \times L_z$ with no flow boundary conditions in the directions lateral to average flow and $L_z = 105, 212$ and 2.5×10^{-4} (lattice units) in the direction of flow.

nonwetting fluid is S_{nc}^{∞} as given earlier for Bo = 0. Determining the exponent μ_h in the scaling $h = \ell_h \mathrm{Bo}^{-\mu_h}$ in terms of standard percolation critical exponents is not obvious and we settle for observing its value from the numerical IP experiments of Fig. 13.

We could equivalently restate the above using the Wilkinson (1984) result of Eq. (37) by saying that a_h (the size of pores being invaded at $z = h$ where defending fjords are being entirely pinched off in all directions) is a function of Bond number and given by

$$a_h(\mathrm{Bo}) = \frac{a_0}{1 + \mathrm{Bo}^{1-\mu_h}}, \tag{41}$$

which behaves properly at Bo = 0 and results in Eqs. (37) and (39) being identical.

For an IP system of lateral dimensions 18 × 105 (the dimensions of our laboratory flow cell), flow-length dimensions of 105, 212 and 2.5×10^4, and no-flow boundary conditions in the lateral directions, we observe in Fig. 13 a slightly different scaling of $h \propto \mathrm{Bo}^{-0.89}$. The no-flow versus periodic lateral boundary conditions may have a slight influence on the exponent. In connecting to lab data, we will use the $h \propto \mathrm{Bo}^{-0.89}$ scaling.

The saturation $s_h = s(h)$ at the point $z = h$ where the residual saturation region begins has been estimated by Wilkinson (1984) in his appendix to scale as

$$s_h = s_{h0} + \tilde{c}_{sh} \left(\frac{\xi}{a_0} \right)^{-(1+\beta)/\nu} \tag{42}$$

$$= s_{h0} + c_{sh} \mathrm{Bo}^{(1+\beta)/(1+\nu)} \tag{43}$$

where the exponent β is a standard exponent of ordinary percolation that controls how the fraction of defending water sites belonging to the infinite cluster of water in regular percolation increases above the percolation threshold s_{h0}. In 3D, $\beta = 0.418$, $\nu = 0.875$ (the correlation-length exponent), while for a cubic IP lattice, $s_{h0} = 0.66$ (Wilkinson, 1984). Note that the only place in the description of the drainage fronts being developed here where ξ is used is in the determination of the nonwetting saturation s_h of the residual saturation region, and we elect to work with Eq. (43) written as $s_h = s_{h0} + c_{sh} \mathrm{Bo}^{\beta_h}$ where

$$\beta_h = \frac{1+\beta}{1+\nu} \tag{44}$$

or $\beta_h = 0.756$ (3D).

3.2.3. Functional form of $s(z)$

In 3D, the local nonwetting fluid saturation profile $s(z)$ observed in IP simulations is constrained by the five observables w, $s_w = s(w)$, $b_w = ds/dz|_{z=w}$, h and $s_h = s(h)$. All of these scale with Bo according to the rules given in the previous subsections. At the point $z = 0$, we expect the slope to be zero and the local curvature to be positive with a monotonically increasing slope until the slope b_w is attained at the inflection point $z = w$. Between $z = w$ and $z = h$, the slope will monotonically decrease until it is zero at $z = h$.

We thus separate the $s(z)$ model into three regions behind the front

$$s(z) = \begin{cases} s_a(z) & \text{for } 0 < z < w \\ s_b(z) & \text{for } w \le z \le h \\ s_h & \text{for } z > h. \end{cases} \tag{45}$$

A simple power law increase for $s_a(z)$ with increasing z does an excellent job matching the numerical (IP) and laboratory observations of the saturation profile,

$$s_a(z) = s_w \left(\frac{z}{w} \right)^{b_w w / s_w}. \tag{46}$$

To find an appropriate functional form for $s_b(z)$, we first write

$$s_b(z) = s_h - (s_h - s_w) f(z) \tag{47}$$

and look for a function $f(z)$ that has a slope $df(z)/dz|_{z=w} = -b_w/(s_h - s_w)$ at $z = w$ and then monotonically transitions to zero slope at $z = h$. This function also must satisfy $f(w) = 1$ and $f(h) = 0$. There are an infinity of functions $f(z)$ that can satisfy these constraints. A challenge is that the shape of the saturation curve between $z = w$ and $z = h$ changes with decreasing Bo. We will give two functions for $f(z)$ that do a reasonable job of matching the numerical and laboratory data.

A first possible functional form is

$$f_1(z) = \left(\frac{h-z}{h-w} \right)^{\frac{b_w(h-w)}{(s_h - s_w)} - \alpha_f} \left[1 + \frac{\alpha_f}{\beta_f} \left(\frac{z-w}{h-w} \right) \right]^{-\beta_f}. \tag{48}$$

Formally, the exponents α_f and β_f can take any value and the constraints on $f(z)$ will be satisfied. We find that a good fit is obtained by taking $\beta_f = 1/3$ for all Bo and taking α_f to be a simple linear function

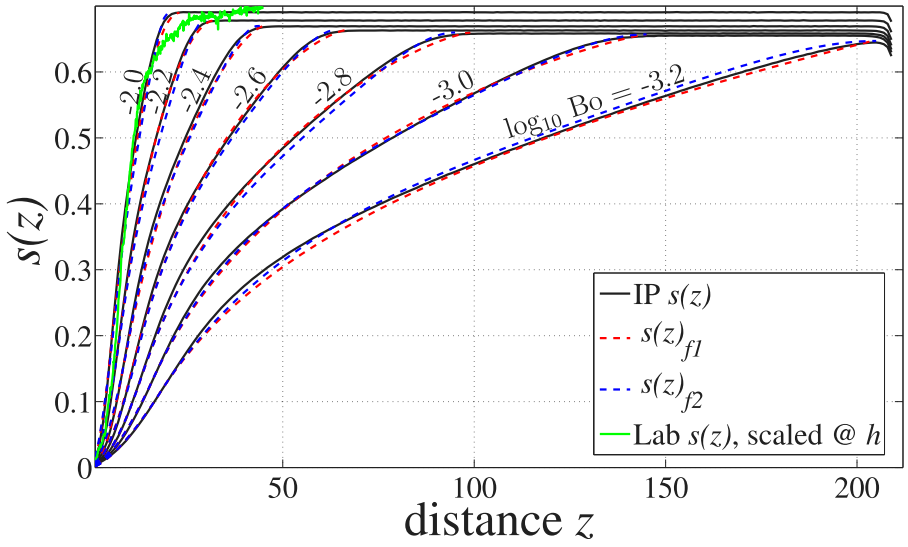

Fig. 14. Saturation profiles ($s(z)$) from IP simulations (black) at variable Bo are plotted alongside the functions given by Eq. (45) with Eqs. (48) (red) and (50) (blue). From left to right, $log_{10}(\mathrm{Bo}) = [-2.0, -2.2, -2.4, -2.6, -2.8, -3.0, -3.2]$. A laboratory observation of $s(z)$ at $log_{10}(\mathrm{Bo}) = -2.1$ (air/water) is shown in green. It is scaled at h to match the predictions of Eqs. (40) and (43).

of the dimensionless ratio w/h, which is a function of Bo as given above

$$\alpha_f = \alpha_{f0}\left(1 - \alpha_{f1}\frac{w}{h}\right). \tag{49}$$

A good fit to the observations is obtained with $\alpha_{f0} = 3.7$ and $\alpha_{f1} = 15.9$. Other, more complicated, nonlinear functions for $\alpha_f(w/h)$ may provide a better fit.

An alternative form with fitting exponents that are independent of Bo is

$$f_2(z) = \frac{(1-c_f)^{\delta_f}}{\left[1-(w/h)^{\beta_f}\right]^{\tau_f}} \frac{\left[1-(z/h)^{\beta_f}\right]^{\tau_f}}{\left[1-c_f(z/w)^{-\alpha_f}\right]^{\delta_f}} \tag{50}$$

where the constant c_f is defined in terms of another constant γ_f as

$$c_f = \frac{\gamma_f}{1+\gamma_f} \tag{51}$$

with

$$\gamma_f = \frac{1}{\delta_f \alpha_f}\left[\frac{w\, b_w}{s_h - s_w} - \tau_f \beta_f \frac{(w/h)^{\beta_f}}{1-(w/h)^{\beta_f}}\right]. \tag{52}$$

It is strictly required that $\tau_f > 1$ in order for the slope to be zero at $z = h$. The other exponents α_f, β_f and δ_f have no constraints. After exploring a range of possibilities, we find that taking $\alpha_f = 0.8$, $\beta_f = \delta_f = 5$ and $\tau_f = 2$ does an adequate job of fitting the IP data as a function of Bo. The fits to the IP data using the above $f_1(z)$ and $f_2(z)$ are shown in Fig. 14.

In either of these two functions $f_1(z)$ and $f_2(z)$, all Bo dependence of the shape of the curves is controlled by the Bo dependence of w and h as given earlier. There certainly exist other functions for $f(z)$ that can fit the data better, but they will have a more complicated form. We will use $f_2(z)$ going forward due to its relative simplicity. We implicitly assume that the $f_2(z)$ exponents $\alpha_f = 0.8$, $\beta_f = \delta_f = 5$ and $\tau_f = 2$ are universal and applicable to any material.

When applying the above model for $s(z)$ to different porous media, the parameters expected to change from material to material are ℓ_h, ℓ_w, c_{sh}, c_{bw}, c_{sw}, s_{h0}, b_{w0}, and w_0, which all depend on the details of the network of pores involved. Conversely, the exponents $\mu = 0.467$, $\mu_h = 0.845$, $\omega = 0.64$, $\beta_w = 0.87$, and $\beta_h = 1.62$ are assumed to have universal values that apply to any 3D porous material. In Fig. 14, we plot $s(z)$ over a range of Bo values in the vicinity of our experiment ($\mathrm{Bo} = 7.4 \times 10^{-3}$). The IP results in black are captured well by the models of $s(z)$ in red and blue. The hydrostatic curve observed in our experiment is re-plotted from Fig. 3 in green, and scaled to match the values of h and s_h predicted by Eqs. (40) and (43). The values of h agree if the lattice spacing is equal to four times our mean grain diameter, which suggests that the percolation node spacing represents the average distance traversed by a meniscus during a Haines jump, rather than the distance between adjacent pores. As shown in Fig. 3, residual water saturation in the experiment is much lower than expected from the IP simulations, which may indicate that thin film flows are an important drainage mechanism at lower water saturation (e.g., Nimmo, 2010). Recently, Ni et al. (2021) coupled IP to a continuum percolation model of thin film flow to simulate cycles of drainage and imbibition.

3.3. Saturation models when Bo > 0 and Ca > 0

Finally, we address the more challenging problem of the capillary number dependence in $s(z)$. When the defending liquid in stable drainage is being extracted from a voxel at a rate where the viscous pressure drop is no longer negligible compared to the capillary pressure drop across a meniscus, Wilkinson (1984) and later Méheustt et al. (2002) note that the gravitational pressure drop is partially undone by the viscous pressure drop.

The viscous pressure gradient is determined from Darcy's law as

$$\frac{\partial P_v}{\partial z} = -\frac{q_w \eta_w}{k_o \kappa_w(S_w)}. \tag{53}$$

One challenge is that it will not be uniform throughout the region $0 \le z \le h$ due to varying saturation, but it must, in general, be numerically determined as part of the dynamic modeling of Eqs. (1) and (2).

However, when considering the 1D experimental observations of $s(z)$, we can estimate the viscous pressure gradient analytically in the following approximate manner. Assume that the saturation profile $s(z)$ is simply advancing through the flow cell with the average flow speed v_z, controlled by the rate of water extraction from the bottom of the cell. This is consistent with our observations and will generally be the case when the hydraulic conductivity is much larger than the Darcy velocity (Hoogland et al., 2015). If we denote the position of the advancing lead menisci at any instant as $z_o(t)$, the approximation is that the saturation profile evolves through time as $s(z,t) = s(z - z_o(t))$, where the function $s(z)$ is again determined from the IP result of Eq. (45), but

with w, ξ and h now satisfying new Ca-dependent scalings. The constant speed of the profile is given by

$$v_z = \frac{dz_o(t)}{dt} = -\frac{1}{\phi}\frac{k_o}{\eta_w}\left.\frac{\partial P_v}{\partial z}\right|_{z\le z_o(t)} \tag{54}$$

where the viscous pressure gradient is assumed to be uniform ahead of the front ($z < z_o(t)$).

The rate at which the water saturation $S_w(z,t)$ is changing can then be approximated as

$$\begin{aligned}\phi\frac{\partial S_w(z-z_o(t))}{\partial t} &= -\phi\frac{\partial S_w(z-z_o(t))}{\partial z}\frac{dz_o(t)}{dt}\\ &= \frac{k_o}{\eta_w}\left.\frac{\partial P_v}{\partial z}\right|_{z\le z_o(t)}\frac{\partial S_w}{\partial z}.\end{aligned} \tag{55}$$

From Eq. (1) for the conservation of water mass in 1D, we also have

$$\begin{aligned}\phi\frac{\partial S_w(z,t)}{\partial t} &= -\frac{\partial q_w(z,t)}{\partial z}\\ &= \frac{k_o}{\eta_w}\frac{\partial}{\partial z}\left[\kappa_w(S_w)\frac{\partial P_v(z,t)}{\partial z}\right]\end{aligned} \tag{56}$$

which upon equating Eqs. (55) and (56) gives

$$\left.\frac{\partial P_v}{\partial z}\right|_{z\le z_o(t)}\frac{\partial S_w(z,t)}{\partial z} = \frac{\partial}{\partial z}\left[\kappa_w(S_w)\frac{\partial P_v(z,t)}{\partial z}\right]. \tag{57}$$

In order to determine how the viscous pressure gradient is varying with z, we consider the moment in time when $z_o(t) = 0$ and integrate from a point z in the profile to h to obtain

$$\begin{aligned}&\left.\frac{\partial P_v}{\partial z}\right|_{z\le 0}\left[S_w(h) - S_w(z)\right] =\\ &\kappa_w(S_w(h))\left.\frac{\partial P_v(z)}{\partial z}\right|_{z=h} - \kappa_w(S_w(z))\frac{\partial P_v(z)}{\partial z}.\end{aligned} \tag{58}$$

Now at $z = h$, the relative permeability of the water goes to zero ($\kappa_w(S_w(h)) = 0$) while $S_w(h) = S_{wc} = 1 - s_h$ is the residual water saturation in the region $z \ge h$. We then obtain the result for the viscous pressure gradient as

$$\frac{\partial P_v(z)}{\partial z} = \left[\frac{S_w(z) - S_{wc}}{\kappa_w(S_w(z))}\right]\left.\frac{\partial P_v}{\partial z}\right|_{z\le 0}. \tag{59}$$

The boundary condition at $z = h$ is that the water's Darcy velocity goes to zero. This is the requirement that $\kappa_w(S_w(z))\partial P_v(z)/\partial z \to 0$ as $z \to h$, which is satisfied by Eq. (59). At $z = 0$, we would like $\partial P_v(z)/\partial z|_{z=0} = \partial P_v/\partial z|_{z\le 0}$. This can be achieved either by selecting $S_w(0)$ to have a particular value less than one, or by assuming $S_w(0) = 1$ and requiring the relative permeability to have the value $\kappa_w(S_w(0)) = 1 - S_{wc}$ at $z = 0$. Either approach gives the same final result in the analysis that follows, but we choose the second option.

To address how the scalings of w, ξ and h depend on the viscous pressure gradient, we note that flow and saturation distribution behind the front are controlled by the gradient in the capillary pressure $\partial P_c/\partial z = \partial P_n/\partial z - \partial P_w/\partial z \approx -\partial P_w/\partial z$, which in the presence of both gravity and finite viscous flow is

$$\frac{\partial P_c(z)}{\partial z} = \Delta\rho g - \left[\frac{S_w(z) - S_{wc}}{\kappa_w(S_w(z))}\right]\left.\frac{\partial P_v}{\partial z}\right|_{z\le 0}. \tag{60}$$

Defining the capillary number Ca as that in the pure liquid ahead of the front

$$\mathrm{Ca} = \frac{a_0^2}{\gamma}\left.\frac{\partial P_v}{\partial z}\right|_{z\le 0} \tag{61}$$

the earlier scaling rules of Eqs. (28), (36) and (38) for w, ξ and h now become

$$w = \ell_w\left[\mathrm{Bo} - A_w\mathrm{Ca}\right]^{-\mu} \tag{62}$$

$$\xi = \ell_\xi\left[\mathrm{Bo} - A_\xi\mathrm{Ca}\right]^{-\mu} \tag{63}$$

$$h = \ell_h\left[\mathrm{Bo} - A_h\mathrm{Ca}\right]^{-\mu_h} \tag{64}$$

where the dimensionless capillary-number "amplification factors" are defined as

$$A_w = \frac{1}{w}\int_0^w \frac{S_w(z) - S_{wc}}{\kappa_w(S_w(z))}\,dz \tag{65}$$

$$A_\xi = \frac{1}{\xi}\int_{h-\xi}^h \frac{S_w(z) - S_{wc}}{\kappa_w(S_w(z))}\,dz \tag{66}$$

$$A_{hw} = \frac{1}{h-w}\int_w^h \frac{S_w(z) - S_{wc}}{\kappa_w(S_w(z))}\,dz \tag{67}$$

$$A_h = \frac{w}{h}A_w + \left(1 - \frac{w}{h}\right)A_{hw}. \tag{68}$$

Inserting Eqs. (65)–(68) into Eqs. (62)–(64) provides a set of three coupled nonlinear equations that must be solved iteratively to find the roots w, ξ and h that are functions of Bo and Ca.

To proceed, we need a particular model for the water's relative permeability. Although the earlier models of van Genuchten and Corey for the water- and gas-phase relative permeability can certainly be employed, it is more consistent to take a percolation perspective (e.g., Kirkpatrick, 1973; DeGennes, 1983) and write the relative permeability function for water in the percolation form

$$\kappa_w(z) = \frac{(S_w(z) - S_{wc})^{t_w}}{(1 - S_{wc})^{t_w - 1}} \quad \text{for} \quad S_{wc} < S_w \le 1 \tag{69}$$

and $\kappa_w = 0$ when $S_w \le S_{wc}$. A similar form can be assumed for the gas phase. This particular expression gives $\kappa(S_w(0)) = 1 - S_{wc}$ if we take $S_w(0) = 1$, which insures that Eq. (59) reduces to the correct expression at $z = 0$. The conductivity exponent t_w has a universal 3D value that has been reported in the range $3/2 < t_w < 2$ (Stauffer and Aharony, 1992), but is generally considered to be close to 2. The residual water saturation has the predicted value of $S_{wc} = 1 - s_h$, where s_h was given earlier by the scaling of Eq. (43).

In order to use the function $s(z)$ of Eq. (45) in the determination of the amplification factors, we write $S_w(z) = 1 - s(z)$ to give the integrand of each amplification factor as

$$\frac{S_w(z) - S_{wc}}{\kappa_w(S_w(z))} = \frac{s_h^{t_w - 1}}{[s_h - s(z)]^{t_w - 1}} \tag{70}$$

which shows that t_w must be less than 2 in order for the amplification factors A_ξ and A_h to remain integrable at $z = h$. The closer that t_w is to 2, the larger the amplification factors will become.

One approach for obtaining the lengths w, ξ and h is to use successive approximations. Beginning with a first guess for A_w, A_ξ and A_{hw}, use Eqs. (62)–(64) to make a first estimate of w, ξ and h, and then use these first estimates in Eqs. (65)–(68) to update the amplification factors, repeating in this manner until the lengths do not change.

3.4. Comparison to laboratory observations

We now compare the above saturation-profile model with the saturation profiles measured optically in our flow cell. To do so, we first determine how the amplification factors and lengths vary with Ca for parameters corresponding to the laboratory experiments. As such, we take $\mathrm{Bo} = 7.4 \times 10^{-3}$, and we set the other free parameters of the model according to the $\mathrm{Ca} = 0$ values of Section 3.2. Fig. 15 shows the results of this calculation with permeability exponent $t_w = 1.5$ and $t_w = 1.6$, and with each length normalized by its low Ca limit. We find the expected result that increasing t_w (though not exceeding 2) increases lengths at any given Ca and causes the lengths to diverge at smaller Ca. We also find that h is more sensitive to Ca than w, and that ξ diverges at relatively small Ca.

In Fig. 16, we use the Ca dependence of w and h to predict the water saturation profiles observed in our flow cell, which are scatter-plotted at 1 cm intervals. These observations were obtained by performing a moving average of $s(z)$ across all video frames for the duration of the flows, each at a unique Ca. For clarity, we show a subset of the experiments ($\mathrm{Ca} = 5 \times 10^{-5}$, $\mathrm{Ca} = 2.5 \times 10^{-4}$, $\mathrm{Ca} = 7.5 \times 10^{-4}$, Ca =

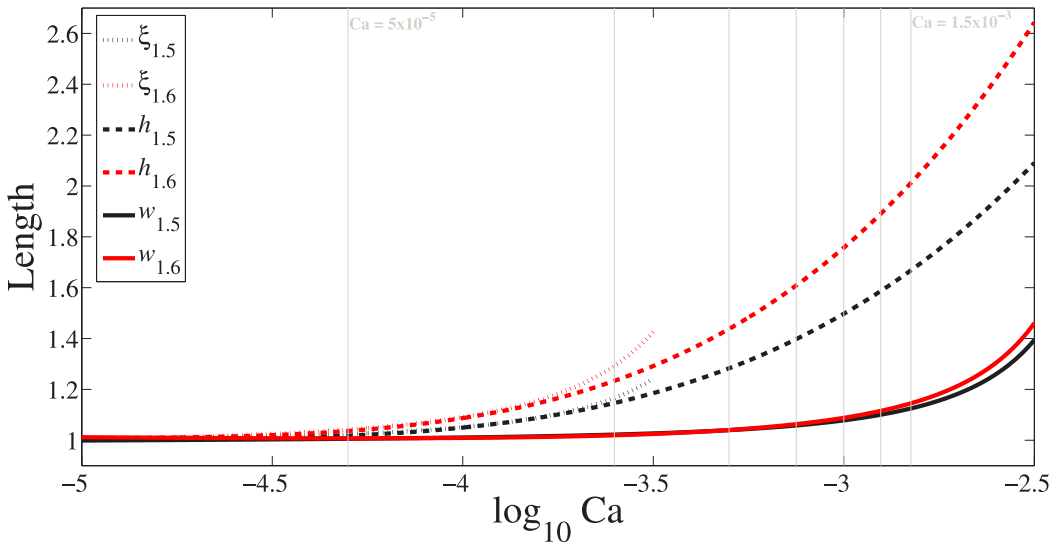

Fig. 15. The lengths w, h, and ξ are plotted as a function of Ca relative to their low Ca limit at two values of the conductivity exponent: $t_w = 1.5$ and $t_w = 1.6$. Gray vertical lines indicate the Ca values of our laboratory experiments.

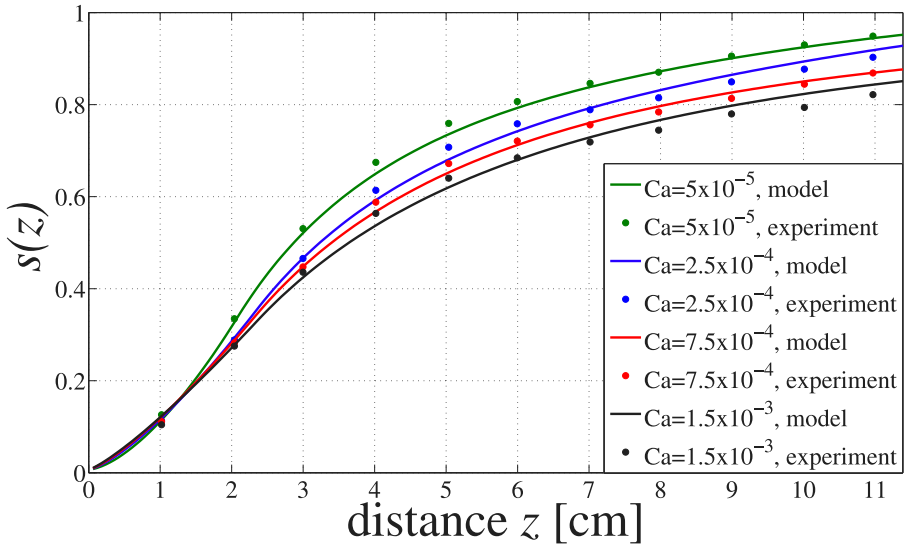

Fig. 16. The model of Eq. (45) is plotted at four Ca values, with Ca-dependent lengths given by Eqs. (62)–(64) (and as plotted in Fig. 15). The value of the conductivity exponent is $t_w = 1.5$. Corresponding observations from laboratory drainage experiments are scattered at 1 cm intervals.

1.5×10^{-3}). The sensitivity of $s(z)$ to small increments of Ca is another good indicator of repeatability. We fit our $s(z)$ model from Eq. (45) to the lowest Ca experiment (Ca = 5.0×10^{-5}) and, keeping s_h fixed, adjust w and h according to the results of Fig. 15 with $t_w = 1.5$.

3.5. The capillary pressure vs. saturation relation

We now obtain the macroscopic relation between the average capillary pressure of a voxel of size L_z located at the point z behind the front

$$\overline{P}_c(z) = \frac{1}{L_z}\int_z^{z+L_z} P_c(z_0)\, dz_0 \tag{71}$$

and the average wetting saturation of the same voxel

$$S_w(z) = 1 - \frac{1}{L_z}\int_z^{z+L_z} s(z_0)\, dz_0. \tag{72}$$

These are thus parametric relations; i.e., letting z run from 0 to h we obtain the entire range of how $\overline{P}_c$ is related to S_w during stable drainage in a gravity field when viscous pressure gradients cannot be neglected.

We begin by using the definitions of the Bond number Bo = $(a_p^2/\gamma)\Delta\rho g$ and capillary number Ca = $(a_p^2/\gamma)\partial P_v/\partial z|_{z\lesssim 0}$ to write the fine-scale (non-averaged) capillary pressure gradient of Eq. (60) as

$$\frac{\partial P_c(z)}{\partial z} = \frac{\gamma}{a_p^2}\left(\mathrm{Bo} - \mathrm{Ca}\left[\frac{s_h}{s_h - s(z)}\right]^{t_w-1}\right). \tag{73}$$

Integrating from the front position $z = 0$ to a distance z and using that at $z = 0$ the entry pressure goes as $P_c(0) = \gamma/a_p$, where a_p is appropriately defined from the Young–Laplace equation $a_p = a_0/(4\cos\theta)$, we obtain the fine-scale capillary pressure which we write in dimensionless form

$$\frac{P_c(z)a_p}{\gamma} = 1 + \frac{z}{a_p}\left\{\mathrm{Bo} - \frac{\mathrm{Ca}}{z}\int_0^z\left[\frac{s_h}{s_h - s(z_0)}\right]^{t_w-1} dz_0\right\} \tag{74}$$

which holds over the range $0 \le z \le h$.

To obtain $\overline{P}_c$ and S_w at each value of z, use the earlier model of Eq. (45) with the lengths w, h and ξ all functions of Bo and Ca to

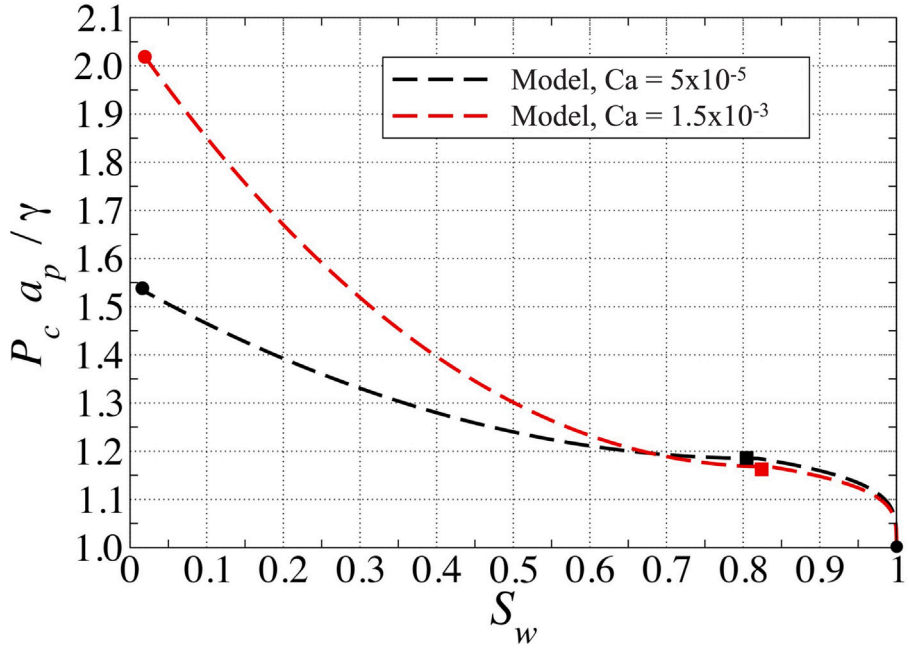

Fig. 17. A plot of $P_c(S_w)$ as normalized by the entry pressure γ/a_p in the case where no averaging over lengths L_z was performed. The shape of the curves is influenced by the shape of the local non-wetting profile $s(z)$ which depends on Bo and Ca through the lengths w, h, and ξ. The circular dots at the end of these curves are the limiting values corresponding to $z = 0$ (the right side in the plot) and $z = h$ (the left side), and the square dots correspond to the inflection at $z = w$.

perform the integrals of the combined Eqs. (71), (72) and (74). Using the parameter values corresponding to the flow-cell experiments, we obtain the capillary pressure relation shown in Fig. 17. In this example, we used the local saturation and capillary pressure values and did not average them over intervals L_z.

In Fig. 17, the end points to the left at highest capillary pressure correspond to points $z \geq h$ and have normalized capillary pressure given by

$$\frac{P_c(h)a_p}{\gamma} = 1 + \frac{h}{a_p}\left(\mathrm{Bo} - \mathrm{Ca}A_h\right) \tag{75}$$

where A_h is the amplification factor of Eq. (68). The capillary pressure at the inflection point $z = w$ (denoted by the squares in the figure) occur at

$$\frac{P_c(w)a_p}{\gamma} = 1 + \frac{w}{a_p}\left(\mathrm{Bo} - \mathrm{Ca}A_w\right). \tag{76}$$

The $P_c(S_w)$ relation of the present model of gravity-stabilized drainage, as depicted in Fig. 17, is distinct from the van Genuchten model in that the end point corresponding $z = h$ represents the residual saturation values that cannot be surpassed, while the end point at $z = 0$ corresponds to the entry pressure γ/a_p. The key points denoted as circular and square dots depend on Bo and Ca as given above, which is also distinct from van Genuchten.

When averaging voxels L_z are of finite size, a final consideration is the relation between $\overline{P}_c$ and S_w in a voxel that is being penetrated by the front but has not yet been percolated. If the front has penetrated a distance ζ into a voxel, we define the top of the voxel being penetrated as $z = \zeta$, the lead menisci at the front as $z = 0$ so that the bottom of the voxel is at $z = -L_z + \zeta$. In the region $0 \leq z \leq \zeta$ both phases percolate, and the local water saturation varies as $P_w(z) = P_n - P_c(z)$ with $P_c(z)$ given by Eq. (74). In the region $-L_z + \zeta \leq z < 0$, there is only water, and the water pressure varies linearly with z as

$$P_w(z) = P_n - \frac{\gamma}{a_p} - \frac{\gamma z}{a_p^2}\left(\mathrm{Bo} - \mathrm{Ca}\right). \tag{77}$$

Thus by averaging over the voxel being penetrated we obtain the parametric relation for how $\overline{P}_c$ is related to S_w in the lead voxel prior to $S_w = 1 - S_{nc}$ being attained

$$\frac{\overline{P}_c(\zeta)a_p}{\gamma} = 1 + \frac{1}{L_z}\left\{\int_{-L_z+\zeta}^{0} dz\,\frac{z}{a_p}(\mathrm{Bo} - \mathrm{Ca}) + \int_0^{\zeta} dz\left(\frac{z\mathrm{Bo}}{a_p} - \frac{\mathrm{Ca}}{a_p}\int_0^z dz_0\left[\frac{s_h}{s_h - s(z_0)}\right]^{t_w - 1}\right)\right\} \tag{78}$$

and

$$S_w(\zeta) = 1 - \frac{1}{L_z}\int_0^{\zeta} s(z)\,dz. \tag{79}$$

By letting ζ vary from 0 to L_z, we obtain the entire range of the $\overline{P}_c(S_w)$ relation appropriate to a lead voxel that is being penetrated prior to percolation.

Further, the critical percolation value of the invading non-wetting fluid when a voxel of length L_z is first traversed is

$$S_{nc} = \frac{1}{L_z}\int_0^{L_z} s(z)\,dz \tag{80}$$

and has dependence on Bo and Ca as prescribed earlier in our model for $s(z)$.

Last, in the limit as $\mathrm{Bo} \to 0$ and $\mathrm{Ca} \to 0$ (for example slow horizontal flow in a thin 2D flow cell), we find that $P_c(S_w) = \gamma/a_p$, which is a simple constant and distinct from the van Genuchten prediction. This has also been predicted and experimentally verified by Moura et al. (2015) for horizontal flow through a cell of single bead thickness. In this case, the saturation left behind in each voxel at percolation is then the S_{nc} of Eq. (19). Implicit in the above is that the pore size a_p is not systematically varying across the length of the flow cell (or local voxel). If there is a gradient in a_p, there will be a simple corresponding gradient in $P_c = \gamma/a_p$, even when $\mathrm{Bo} \approx 0$ and $\mathrm{Ca} \approx 0$.

4. Conclusion

Stable drainage experiments have been performed (air invading water-saturated glass beads in a 3D flow cell) while optically measuring the 2D spatial distribution of saturation (the optical transmission measurements averaged over the width of the cell). The measurements

show that the saturation profile $s(z)$ is dependent on the capillary number Ca, with larger Ca producing more extended saturation profiles. Invasion percolation simulations demonstrate the effect of variable Bo on $s(z)$. In order to explain these observations, a percolation-based model was developed. A scaling form for the saturation versus distance relation was proposed with profile shape exponents determined from Invasion Percolation numerical experiments. This form has explicit dependence on two key lengths: w, the width of the invasion front, defined here as the inflection point where the saturation profile goes from positive to negative curvature, and h, the width of the entire region behind the front where both fluid phases percolate. A third length ξ, defined as the maximum size of trapped water clusters in the residual saturation region $z > h$, more weakly influences the residual water saturation. All three lengths w, h and ξ are shown to have both Bo and Ca dependence.

The critical nonwetting saturation S_{nc} at which a voxel at the front is first percolated was optically measured and shown to depend on the size of the voxel L_z, as well as on Bo and Ca. The main contribution of this work is a model for $s(z)$ which can be used to determine $S_{nc}(\mathrm{Bo}, \mathrm{Ca}, L_z)$. It applies to stable drainage scenarios and will be useful for macroscopic porous-continuum modeling of two-phase flow. We also show how the theoretical model for $s(z)$ produces the macroscopic capillary pressure function $P_c(S_w, \mathrm{Bo}, \mathrm{Ca})$ for use in macroscopic flow modeling.

Declaration of competing interest

The authors declare that they have no known competing financial interests or personal relationships that could have appeared to influence the work reported in this paper.

Acknowledgments

This material is based upon work supported by the U.S. Department of Energy, Office of Science, United States, Office of Basic Energy Sciences, Chemical Sciences, Geosciences and Biosciences Division under Contract DE-AC-2–5CH11231. The second author, SRP, would like to thank Renaud Toussaint for interesting conversations on these topics over the years. The work of Yder Masson was partially supported by the consortium I-SITE E2S/UPPA/THERMapp.

Appendix

See Table A.1.

Table A.1
A table of symbols and notation, approximately in order of appearance.

S_w	Wetting phase saturation []
S_{nw}	Nonwetting phase saturation []
$\tilde{S}$	Normalized saturation []
S_{nc}	Critical nonwetting saturation []
S_{wc}	Residual wetting saturation []
L_z	Voxel length [L]
L_x, L_y	Voxel lateral dimensions [L]
Bo	Bond number []
Ca	Capillary number []
Re	Reynolds number []
ϕ	Porosity []
ρ	Density [ML^{-3}]
$\boldsymbol{q}$	Darcy velocity [LT^{-1}]
k_o	Permeability [L^2]
κ	Relative permeability []
η	Viscosity [$\mathrm{ML}^{-1}\mathrm{T}^{-1}$]
P	Fluid pressure [$\mathrm{ML}^{-1}\mathrm{T}^{-2}$]
P_c	Capillary pressure [$\mathrm{ML}^{-1}\mathrm{T}^{-2}$]
P_0	van Genuchten entry pressure [$\mathrm{ML}^{-1}\mathrm{T}^{-2}$]
a_0	Characteristic pore size [L]
$\boldsymbol{g}$	Acceleration of gravity [LT^{-2}]
γ	Surface tension [MT^{-2}]
d_{50}	Median grain size [L]
τ	Light transmittance []
n	Refractive index []
k	Number of pores traversed by light []
I	Light intensity [C]
I_o	Intensity of the light source [C]
I_a, I_w	Air (a) and water (w)-saturated light intensity [C]
$\tilde{I}$	Normalized light intensity []
α	Light absorption coefficient []
d_p	Average pore diameter [L]
d_{cam}	Image averaging height [L]
d_{width}	Image averaging width [L]
λ	van Genuchten fitting parameter []
IP	Invasion Percolation
V_{nc}^{∞}	Injected volume at percolation [L^3]
S_{nc}^{∞}	Injected saturation at percolation []
D_c	Fractal dimension []
d	Euclidean-space dimension []
N	Number of lattice sites []
s	Nonwetting saturation []
$w_o, \epsilon_1, \epsilon_2$	Bo = 0 $s(z)$ fit parameters
f_w	Proportionality constant between s_w and S_{nc}^{∞} []
w	Distance to inflection point in $s(z)$ [L]
s_w	Nonwetting saturation at w []
h	Distance to residual in $s(z)$ [L]
s_h	Nonwetting saturation at h []
ξ	Maximum cluster size in the defending phase [L]
b_w	The slope of $s(z)$ at w [L^{-1}]
q	Nonwetting phase occupation probability []
q_c	Percolation threshold []
π	Entry pressure distribution []
W_l	Entry pressure distribution width []
ν	Correlation length divergence exponent []
μ	$= \nu/(1+\nu)$ []
ℓ_w	Proportionality constant in w(Bo) [L]
Bo_t	Transitional Bo []
β_w	s_w(Bo) exponent []
w_0	Low Bo limit of w [L]
c_{sw}	Proportionality constant in s_w(Bo) []
s_{w0}	Low Bo limit of s_w []
ω	b_w(Bo) exponent []
c_{bw}	Proportionality constant in b_w(Bo) []
b_{w0}	Low Bo limit of b_w [L^{-1}]
ℓ_ξ	Proportionality constant in ξ(Bo) [L]
a_h	Characteristic wetting-saturated pore size at h [L]
μ_h	h(Bo) exponent []
ℓ_h	Proportionality constant in h(Bo) [L]
s_{h0}	Low Bo limit of s_h []
c_{sh}	Fitting constant in s_h(Bo) []
β_h	s_h(Bo) exponent []
s_a	Nonwetting saturation in the region $0 < z < w$ []
s_b	Nonwetting saturation in the region $w \le z \le h$ []
f, f_1, f_2	Curvature functions in s_b []
$\alpha_f, \beta_f, \delta_f, \tau_f$	Fitting exponents in f, f_1, f_2 []
c_f, γ_f	Constants in f_2 []
v_z	Translational velocity of $s(z)$ profile [LT^{-1}]
z_o	Position of lead menisci (leading tip of $s(z)$) [L]
A_w, A_ξ, A_{hw}, A_h	Amplification factors controlling $s(z)$ distortion at nonzero Ca []
t_w	Conductivity exponent []

(continued on next page)

Table A.1 (*continued*).

References

Abu-Al-Saud, M.O., Riaz, A., Tchelepi, H.A., 2017. Multiscale level-set method for accurate modeling of immiscible two-phase flow with deposited thin films on solid surfaces. J. Comput. Phys. 333, 297–320.

Armstrong, R.T., Evseev, N., Koroteev, D., Berg, S., 2015. Modeling the velocity field during haines jumps. Adv. Water Resour. 77, 57–68.

Birovljev, A., Furuberg, L., Feder, J., Jssang, T., Måløy, K.J., Aharony, A., 1991. Gravity invasion percolation in two dimensions: Experiment and simulation. Phys. Rev. Lett. 67 (5), 584–587.

Corey, A.T., 1954. The interrelation between gas and oil relative permeabilities. Prod. Mon..

Cottin, C., Bodiguel, H., Colin, A., 2010. Drainage in two-dimensional porous media: From capillary fingering to viscous flow. Phys. Rev. E 82 (4), 046315.
DeGennes, P.G., 1983. Theory of slow biphasic flows in porous media. Physicochem. Hydrodynam. 4, 175–185.
Dury, O., Fischer, U., Schulin, R., 1999. A comparison of relative nonwetting-phase permeability models. Water Resour. Res. 35 (5), 1481–1493.
Frette, O.I., Måløy, K.J., Schmittbuhl, J., Hansen, A., 1997. Immiscible displacement of viscosity-matched fluids in two-dimensional porous media. Phys. Rev. E 55, 2969–2975.
van Genuchten, M.T., 1980. A closed-form equation for predicting the hydraulic conductivity of unsaturated soils. Soil Sci. Soc. Am. J. 44, 892–898.
Ghanbarian, B., Sahimi, M., Daigle, H., 2016. Modeling relative permeability of water in soil: Application of effective-medium approximation and percolation theory. Water Resour. Res. 52 (7), 5025–5040.
Glass, R.J., Conrad, S.H., Peplinski, W., 2000. Gavity-destabilized nonwetting phase invasion in macroheterogeneous porous media: Experimental observations of invasion dynamics and scale analysis. Water Resour. Res. 36 (11), 3121–3137.
Gray, W.G., Miller, C.T., 2014. Introduction To the Thermodynamically Constrained Averaging Theory for Porous Medium Systems. Springer.
Hassanizadeh, S., Gray, W.G., 1990. Mechanics and thermodynamics of multiphase flow in porous media including interphase boundaries. Adv. Water Resour. 13 (4), 169–186. http://dx.doi.org/10.1016/0309-1708(90)90040-B.
Hoogland, F., Lehmann, P., Or, D., 2015. The formation of viscous limited saturation zones behind rapid drainage fronts in porous media. Water Resour. Res. 51 (12), 9862–9890.
Kirkpatrick, S., 1973. Percolation and conduction. Rev. Modern Phys. 45, 574–586.
Lenormand, R., Touboul, E., Zarcone, C., 1988. Numerical models and experiments on immiscible displacements in porous media. J. Fluid Mech. 189.
Løvoll, G., Meheust, Y., Maloy, K., Aker, E., Schmittbuhl, J., 2005. Competition of gravity, capillary and viscous forces during drainage in a two-dimensional porous medium, a pore scale study. Energy 30, 861–872.
Masson, Y., 2016. A fast two-step algorithm for invasion percolation with trapping. Comput. Geosci. 90, 41–48.
Méheustt, Y., Løvoll, G., Måløy, K.J., Schmittbuhl, J., 2002. Interface scaling in a two-dimensional porous medium under combined viscous, gravity, and capillary effects. Phys. Rev. E 66, 051603.
Moura, M., Florentino, E.-A., Måløy, K.J., Schafer, G, Toussaint, R., 2015. Impact of sample geometry on the measurement of pressure-saturation curves: Experiments and simulations. Water Resour. Res. 51, 8900–8926. http://dx.doi.org/10.1002/2015WR017196.
Ni, H., Møyner, O., Kurtev, K.D., Benson, S.M., 2021. Quantifying CO2 capillary heterogeneity trapping through macroscopic percolation simulation. Adv. Water Resour. 155.
Nimmo, J.R., 2010. Theory for source-responsive and free-surface film modeling of unsaturated flow. Vadose Zone J. 9, 295–306.
Pruess, K., 2004. The TOUGH codes - a family of simulation tools for multiphase flow and transport processes in permeable media. Vadose Zone J. 3 (3), 738–746.
Reynolds, C.A., Menke, H., Andrew, M., Blunt, M.J., Krevor, S., 2017. Dynamic fluid connectivity during steady-state multiphase flow in a sandstone. Proc. Natl. Acad. Sci. 114 (31), 8187–8192.
Rosso, M., Gouyet, J.F., Sapoval, B., 1985. Determination of percolatiuon probability from the use of a concentration gradient. Phys. Rev. B 32, 6053–6054.
Stauffer, D., Aharony, A., 1992. Introduction To Percolation Theory. Taylor Francis, London.
Tidwell, V.C., Glass, R.J., 1994. X ray and visible light transmission for laboratory measurement of two-dimensional saturation fields in thin-slab systems. Water Resour. Res. 30 (11), 2873–2882.
Toussaint, R., Måløy, K., Méheust, Y., Løvoll, G., Jankov, M., Scheäfer, G., Schmittbuhl, J., 2012. Two-phase flow: Structure, upscaling, and consequences for macroscopic transport properties. Vadose Zone J. 11 (3).
Wilkinson, D., 1984. Percolation model of immiscible displacement in the presence of buoyancy forces. Phys. Rev. A 30, 520–531.
Wilkinson, D., Willemsen, J.F., 1983. Invasion percolation: a new form of percolation theory. J. Phys. A: Math. Gen. 16, 3365–3376.
Yortsos, Y.C., Xu, B., Salin, D., 2001. Delineation of microscale regimes of fully-developed drainage and implications for continuum models. Comput. Geosci. 5 (3), 257–278.